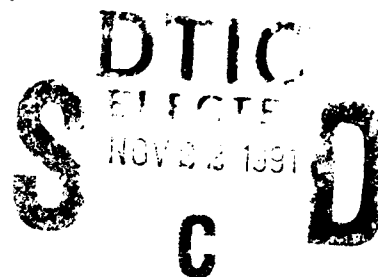AD-A244 458

PL-TR-91-2164

A COMPARISON OF SYSTEMATIC ERRORS IN AFGL AND COLA FORECAST MODELS

Anandu D. Vernekar
Jiayu Zhou
Benjamin Kirtman

University of Maryland
Department of Meteorology
College Park, Maryland 20742

June 1991

Final Report
8 March 1988-8 May 1991

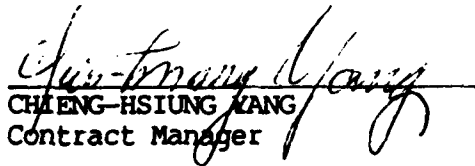APPROVED FOR PUBLIC RELEASE; DISTRIBUTION UNLIMITED

PHILLIPS LABORATORY
AIR FORCE SYSTEMS COMMAND
HANSCOM AIR FORCE BASE, MASSACHUSETTS 01731-5000

91-15863

91 1118 093

This technical report has been reviewed and is approved for publication.

CHIENG-HSIUNG YANG
Contract Manager

H. STUART MUENCH
Acting Branch Chief

DONALD D. GRANTHAM, Acting Director
Atmospheric Sciences Division

This document has been reviewed by the ESD Public Affairs Office (PA) and is releasable to the National Technical Information Service (NTIS).

REPORT DOCUMENTATION PAGE

1. AGENCY USE ONLY (Leave blank)	2. REPORT DATE June 1991	3. REPORT TYPE AND DATES COVERED Final Report (8 Mar 1988–8 May 1991)

4. TITLE AND SUBTITLE A Comparison of Systematic Errors in AFGL and COLA Forecast Models	5. FUNDING NUMBERS PE 61102F PR 2310 TA G7 WU DC Contract F19628-88-K-0015

6. AUTHOR(S) Anandu D. Vernekar Jiayu Zhou Benjamin Kirtman	

7. PERFORMING ORGANIZATION NAME(S) AND ADDRESS(ES) University of Maryland Department of Meteorology College Park, Maryland 20742	8. PERFORMING ORGANIZATION REPORT NUMBER

9. SPONSORING/MONITORING AGENCY NAME(S) AND ADDRESS(ES) Phillips Laboratory Hanscom AFB, Massachusetts 01731-5000 Contract Manager: Chien-Hsiung Yang/LYP	10. SPONSORING/MONITORING AGENCY REPORT NUMBER PL-TR-91-2164

11. SUPPLEMENTARY NOTES

12a. DISTRIBUTION/AVAILABILITY STATEMENT Approved for public release; distribution unlimited	12b. DISTRIBUTION CODE

13. ABSTRACT (Maximum 200 words) Forecast errors exhibit the characteristics of approximations in simulating dynamical and physical processes in models. The models are very complex and hence it is not always possible to identify the approximations responsible for any particular error pattern in forecasts. A comparison between the models' forecast performances can be valuable in isolating the causes of error patterns. Here a comparison of forecast errors in the AFGL and COLA models is made with the intent of identifying the causes of forecast errors. The two models are based on identical approximations in simulating the dynamical processes and only minor differences in parameterizations of the physical processes. Nine ten-day forecasts are made to study the error characteristics in the two models. The errors in the 500 mb geopotential height are negative in tropics and positive in extratropics. The temperatures at 850 mb are colder than observed in tropics and warmer than observed in extratropics. At 150 mb the temperatures are warmer than observed in tropics and colder than observed in extratropics. These qualitative error characteristics are not only common to these two models, but also they are common in the NMC, GFDL and ECMWF forecast models. The difference in the error structure between the two models is the magnitude of the error in tropics. The tropical error in the AFGL model is

14. SUBJECT TERMS Systematic errors, AFGL global spectral model, COLA general circulation model, comparison of systematic errors, silhouette orography, gravity wave drag parameterization.	15. NUMBER OF PAGES 82
	16. PRICE CODE

17. SECURITY CLASSIFICATION OF REPORT Unclassified	18. SECURITY CLASSIFICATION OF THIS PAGE Unclassified	19. SECURITY CLASSIFICATION OF ABSTRACT Unclassified	20. LIMITATION OF ABSTRACT SAR

Cont of Block 13:

larger than that in the COLA model. Another difference is in the 850 mb relative
humidity field.   In the AFGL model,relative humidity errors are negative largely
over the ocean and positive over land with minor exceptions.   This error structure
differs from that of the COLA model which consists of mostly positive errors every-
where with some small regions of negative errors. The major differences in the
physical parameterizations between the two models is in the radiation interaction
with deep convective clouds, the manner in which the sea surface temperature (SST)
is prescribed and the vertical transport of heat and moisture by shallow convection.
The magnitude of tropical errors in the geopotential height is 500 mb and temperature
at 850 mb may be because the AFGL model does not include deep convective cloud-
radiation interactions.   The 850 mb relative humidity errors over oceans are probably
due to the manner in which the SST is prescribed and the lack of proper vertical
transport of moisture by the shallow convection parameterization.

ACKNOWLEDGEMENT

Preface

The purpose of the research carried out under the contract No. F19628–88–K–0015 was to determine the impact of orographic effects on the short and medium–range forecasts with the AFGL–GSM. The orographic effects include large scale blocking effects of massive mountain ranges over the globe and the subgrid scale effects of mountains of width of about 50 km on the large scale flow. The large scale blocking effects are represented by the silhouette orography. The subgrid scale effects are the effects of orographic gravity wave drag. The gravity waves aid in transferring momentum between the earth's surface and the atmosphere. This exchange could be in all levels of the troposphere and in the stratosphere. The impact of the orographic effects and of horizontal resolution on the short and medium range forecasts were studied on an earlier version of the AFGL model. The results were reported in Zhou (1990). The parameterization of gravity wave drag in this study was based on a linear theory. The impact of gravity wave drag parameterization based on nonlinear theory was reported in Kirtman et al. (1991). Now the silhouette orography and the gravity wave drag parameterization based on nonlinear theory are implemented in the current version of the AFGL model. The gravity wave drag parameterization was also implemented in the COLA (Center for Ocean–Land–Atmosphere Interactions) model. The purpose of this report is to present a comparison of medium–range forecast performances of the AFGL model with that of the COLA model with the intent of identifying the deficiencies in simulating dynamical and physical processes.

TABLE OF CONTENTS

1. INTRODUCTION

Accuracy of numerical weather prediction is limited by the approximations in the predictive system and the errors in determining the initial state of the atmosphere. In a perfect predictive system the accuracy of the forecast would deteriorate with time due to nonlinear interactions (Lorenz, 1969) and hydrodynamical instabilities (Leith, 1971) so long as there is a non–zero error in the initial state. The rate at which the forecast deteriorates depends on the growth rate of instabilities, the nature of nonlinear interactions and the amplitude and structure of the initial error. The total forecast error is the difference between the forecast and the observation and is commonly measured by the difference between the forecast and the analysis at the verification time. The total forecast error is therefore due to both the imperfections in the predictive system and the error in the initial state. An ensemble average of the total forecast errors based on a large number of forecasts made with synoptically independent initial conditions is referred to as the systematic error. For any particular day's forecast the difference between the mean square of the total error and the mean square of the systematic error is referred to as the mean square of the transient error. The systematic error is usually considered to be due to imperfections in the model; however, the systematic errors and the transient errors are not decoupled in any model.

A large number of studies have been made to identify the spatial structure of systematic errors (see, e.g., Fawcett, 1969; Hollingsworth *et al.* 1980; Wallace and Woessner, 1981; Arpe and Klinker, 1986; among others). The systematic errors in models usually have coherent patterns in space. These geographically fixed error patterns largely change in amplitude with the increase in forecast time. The coherent structures of the systematic errors appear in zonally symmetric fields as well as in the zonally asymmetric fields. In a comprehensive study comparing wintertime systematic errors in the ECMWF (European Centre for Medium Range Weather Forecasts) and the GFDL (Geophysical

1

Fluid Dynamics Laboratory) forecast models, Hollingsworth *et al.* (1980) estimated that the systematic error accounts for more than one third of the total error in medium–range forecasts. Hence, a significant improvement can be made in the forecast skill by reducing the systematic error. Assuming that the growth rate of systematic error was linear Miyakoda *et al.* (1986) suggested that the forecast can be improved by subtracting the systematic error patterns from the forecast fields. Schemm and Faller (1986) proposed a scheme to statistically correct the forecast during integration from empirical relationships between the model variables and the systematic errors. These procedures are only stop gap measures before we identify the deficiencies in the representations of dynamical and physical processes responsible for the systematic errors and improve the representations of these processes.

Bettge (1983) showed that the systematic errors in the 500 mb geopotential height forecasts from ECMWF and NMC (National Meteorological Center) models have similar patterns in that, negative error patterns are observed over the Rockies, the Alps and the Himalayan mountain ranges. He argued that the negative errors are due to the model orography because it is computed by averaging over the model grid which underestimates the height of high mountains. He considered the conservation of potential vorticity of the flow when passing over the model orography. As the vertical extent of the atmosphere is decreased over the top of mountain an anticyclonic vorticity is generated to conserve the potential vorticity. If the model mountains are shallow compared to that of the earth, the model will not generate as much anticyclonic vorticity and that will result in the negative errors. Wallace *et al.* (1983) enhanced the model orography by adding a constant multiple of the orographic standard deviation to the mean orography. The standard deviation of orography was computed from a high resolution orography data. They showed that the enhanced orography in the model reduces the systematic error in the vicinity of the mountain ranges.

Recently, when horizontal and vertical resolutions were increased, new systematic errors were identified which were absent in the low resolution models. The errors were positive in the midlatitude zonally-averaged zonal wind. Also, there were negative errors in the high-latitudes zonally-averaged temperature especially in northern hemisphere winter. In the low resolution models both the surface drag over the mountains and the horizontal momentum flux convergence into the middle and high latitudes in the upper and lower stratosphere by eddies were underestimated. In these models, the simulated northern hemispheric westerly jet agreed well with observations but the southern hemispheric jet was slightly weak. When the horizontal resolution increased the effects of explicitly resolved eddies was to increase the horizontal momentum flux convergence. This increased the strength of the westerly jet in the northern hemisphere but the southern hemispheric westerly jet was in good agreement with observations. The cold temperature bias in high latitudes was consistent with the positive westerly bias to approximately maintain the thermal wind relation. One way of reducing the positive westerly bias is to increase the dissipative processes of zonal momentum in the northern hemisphere winter. Lilly (1972) proposed that the dissipative role of orographically induced gravity waves was important enough to include their effects explicitly in the numerical weather prediction models and the general circulation models. A large number of studies have now shown that the explicit representations of the effect of gravity wave drag in the model reduce the westerly bias in the zonal wind and the cold bias in the temperature (see e.g., Palmer *et al.* (1989); Helfand *et al.* (1987); McFarlane (1987); Iwasaki *et al.* (1989); Kirtman *et al.* (1991))

Determining the spatial structure of the systematic error field is a straightforward procedure; however, it is not obvious how to associate the error field with the physical or dynamical approximations in the model. A comparison between the results of different models as they relate to the real atmosphere can provide us with clues to isolate the causes of errors so that further improvements in the parameterizations can be made to reduce the forecast errors.

The purpose of this study is to compare the systematic errors of the AFGL and COLA forecast models with the intent of isolating the causes of errors so that they can be reduced by improved parameterization. The next section gives a brief comparison of the two models' dynamical and physical parameterizations. The third section explains the experiments and analysis procedure. The fourth section discusses the results. A summary and conclusions are presented in the fifth section.

2. FORECAST MODELS

Both the AFGL and COLA forecast models owe their numerical frame of the dynamics to the NMC spectral model of Sela (1980). Therefore, the simulation of atmospheric dynamical processes are identical. The large scale as well as subgrid scale orographic effects are treated in the same manner in both models. Both models include physical parameterizations of planetary boundary layer, shallow convection, deep moist convection, diurnal variations and cloud–radiation interactions. The only difference between the two models is the representations of these physical parameterizations. Here we shall describe briefly the treatment of dynamics and differences in the representations of the physical processes.

The dynamics of the model is based on the primitive equations. The prognostic equations prescribe the time changes of vorticity, divergence, thermodynamic energy, continuity of water vapor and natural log of surface pressure. Vertical σ–velocity and geopotential height are computed from diagnostic equations. The variables are represented by spherical harmonics with rhomboidal truncation at wave number 30. The horizontal transform grid is equally spaced in the east–west direction with 96 grid points along the latitude circle. In the north–south direction, there are 80 points on the Gausian grid. The horizontal resolution is therefore approximately 2.25° x 3.75° lat–long grid. Vertical coordinate is $\sigma = p/p_*$ where p_* is the surface pressure. There are 19 levels in the vertical

4

The levels are spaced in vertical as 1.00, 0.99, 0.973, 0.948, 0.893, 0.82, 0.735, 0.642, 0.546, 0.45, 0.40, 0.35, 0.30, 0.25, 0.20, 0.15, 0.10, 0.05, 0.00 in σ. The semi–implicit integration is used with 15 minute time interval. The horizontal diffusion in the model is scale selective that is, $k\nabla^4 F$, where F is a prognostic variable. The values of the diffusion constant, k, and the manner in which the diffusion term is used for the prognostic variables differs in the two models. In the AFGL model diffusion term is applied to all modes of the divergence but for the vorticity, temperature and specific humidity it is applied only to modes in the upper half of the rhomboid. The magnitude of the diffusion constant is the same in both cases, which is $k = 6 \times 10^{15}$ m^4 sec^{-1}. In the COLA model k is computed from $k = \left[\frac{a^2}{(N(N+1))}\right]^2/\tau$ where a is the radius of the earth. N is the highest wave number resolved, that is, $N = 30$ in this model. τ is the dissipation time in seconds. For the divergence τ is 21 minutes and for the vorticity, temperature and specific humidity τ is 28 minutes. Hence, the value of k is 2.5×10^{16} for the divergence and 1.9×10^{16} for the vorticity, temperature and specific humidity.

The large scale orography effects are simulated by the silhouette orography. It is computed from the global 10–minute elevation data from the U.S. Navy. At any grid point the silhouette orography is computed as an average of maximum peaks in profiles of mountains in the east–west and north–south directions over the grid box (see, Appendix A). Silhouette orography enhances the topography in a similar manner as in the envelope orography but yields a smoother surface than the envelope orography especially in regions of large subgrid scale variance in a narrow zone, along the southern edge of Tibetan plateau, for example. There is a slight difference between the silhouette orographies in the two models. In the AFGL model the spectral form of the orography was smoothed (see, Appendix a) to reduce the amplitude of the Gibbs oscillations over ocean. In the COLA model no smoothing was applied.

Depending on the atmospheric stability, the gravity waves induced by the subgrid scale orography propagate vertically until they are dissipated in the critical layer or as a

5

consequence of convective and shear instabilities. These waves transport horizontal momentum upward and deposit this momentum where the waves are ultimately dissipated. The momentum is lost by the large scale where the waves are dissipated and it is brought down to the earth surface where it is deposited. The parameterization of these effects consist of surface wave drag and the vertical distribution of the wave drag. The surface wave drag is parameterized by following the procedure suggested by Pierhumbert (1987) and the vertical variation is parameterized according to Palmer *et al.* (1986) and Helfand *et al.* (1987) (see, Appendix B for methodology and Appendix C for computer code).

The atmosphere exchanges momentum, heat and water vapor with the earth's surface in the planetary boundary layer. This exchange depends on the surface cover. Over land, the earth may be covered by snow, ice, and a variety of different plants, sands and soils. Over the ocean, the surface characteristics are determined by sea ice and spatially varying sea surface temperature. In the AFGL model, the planetary boundary over land consists of three parts: soil layer, surface layer and turbulent mixed layer. The soil layer exchanges heat and water vapor with the surface layer. The surface layer exchanges heat, momentum and water vapor with the planetary boundary layer. In the soil layer, heat is transferred by diffusion and water by diffusion and gravitational transport (see, Mahrt and Pan, 1984). Surface fluxes of heat, momentum and water vapor are represented by similarity theory according to Louis (1979). The turbulent mixed layer grows in height due to the surface heating and wind shear (Troen and Mahrt, 1986). The formulation is based on bulk similarity considerations. The depth of the layer is represented in terms of modified bulk Richardson number. Over oceans, the surface layer and the turbulent mixed layer parameterizations are the same as over land but, unlike over land, there is no subsurface layer.

The COLA model planetary boundary layer over land is based on similar considerations. It also consists of three layers: soil layer, surface layer and turbulent mix layer. In this model the effects of the soil layer and the vegetation cover is treated by

6

taking into account physiological and biological processes by a biosphere model (Sellers et al., 1986). In the surface layer the aerodynamic resistances for momentum, sensible and latent heat transfer between the earth's surface and the atmosphere are based on the Monin–Obukhov similarity theory (Miyakoda and Sirutis, 1987). The turbulent mixed layer which varies in height is based on level 2 second–order closure model of Mellor and Yamada (1982). Over oceans, the surface layer and the turbulent mixed layer parameterizations are the same as over land. There is no subsurface layer.

The precipitation due to large–scale supersaturation and subgrid scale moist convection are simulated in both the models. The precipitation occurs in a grid box if the moist air is cooled such that relative humidity exceeds 100%. However the precipitation occurring in a higher level may not all reach the earth's surface. The falling precipitation may evaporate if the lower model layers are dry. The deep moist convective precipitation occurs if there is a moisture flux convergence and the atmospheric column is conditionally unstable. The shallow convection predominantly occurs in undisturbed flow in absence of large scale moisture flux convergence. The trade wind cummuli under a subsidence inversion, daytime convection over land are typical examples of shallow convection. The shallow convection transfers heat, momentum and moisture from boundary layer to the free atmosphere. For deep moist convective precipitation the AFGL model uses Kuo's scheme (Kuo 1965, 1974) modified by Krishnamurti et al. (1976) whereas the COLA model uses Kuo's scheme modified by Anthes (1977). For shallow convection the AFGL model uses a semi–empirical formula derived from GATE data (Mahrt et al., 1987). The COLA model implements the scheme of Tiedtke (1983) which enhances the vertical diffusion of heat and momentum if the levels near the surface are conditionally unstable.

Both models include interaction between radiation and model–generated clouds. A broad band emissivity approach in solar and longwave radiation in presence of clouds by Liao and Ou (1981) is implemented in the AFGL model. According to their altitude, high, middle, and low clouds can form if the model generated relative humidity exceeds a

7

pre–selected critical value as suggested by Geleyn (1981). Middle and low clouds are considered optically black whereas high clouds are half black. Convective clouds and their interaction with radiation are not included in the AFGL model. The COLA model implements the longwave radiation scheme of Harshvardhan et al. (1987) and shortwave radiation scheme of Lacis and Hanson (1974). Two types of clouds, convective clouds and supersaturation clouds, are generated in the model following a procedure similar to that of Slingo (1980, 1987) (see, Hou, 1990). The supersaturation clouds divided into three types, high, middle and low according to their altitude. The supersaturation cloud amounts are determined from the model generated relative humidity and vertical velocity. Deep convective cloud amount is determined from the convective rainfall rate predicted by the Kuo (1974) convective parameterization. The optical properties of clouds are determined from liquid water content and cloud temperature.

In the AFGL model the following quantities are prescribed: the sea surface temperature (SST) from FGGE data for the month of January, roughness length, surface albedo, estimated snow depth and soil moisture content for the first and second layer. Surface specific humidity is set equal to zero in this study. Canopy wetness is also set equal to zero. Soil temperature at 3 meter deep is constant in time but varies from place to place.

For the COLA model the SST is prescribed from NMC data. The biosphere model computes roughness and surface albedo. But, type of vegetation cover is prescribed from climatology for the month. Soil moisture and snow cover are prescribed initially but they are predicted in the model. Sea ice is prescribed from NMC analyses.

There is also a difference in the manner in which SST is prescribed in the two models. In the AFGL model SST is prescribed at all ocean grid points without any changes. In the COLA model the SST is modified depending on the height of the $\sigma = 1$ surface over the oceans. $\sigma = 1$ level in the model is determined by the prescribed orography in the spectral form. However due to the Gibbs oscillations there are non zero height values for $\sigma = 1$

8

level over the oceans. These non zero values could be as much as 1/2 km above or below the sea level. The SST values over ocean are modified assuming a uniform 6.5° K/km lapse rate everywhere. For example, if the height of $\sigma = 1$ level over ocean is ±100m the prescribed SST is modified by adding ∓0.65° K to SST analysis form observations. This modification improves the simulation of heat and moisture fluxes at the ocean surface.

3. EXPERIMENTS AND ANALYSIS

We have made nine medium–range forecasts with both the AFGL and COLA models. NMC analysis was used for initialization and forecast verification. The nine dates were chosen from January 1990 data. The sample size of nine appears reasonable for the study of systematic errors for medium–range forecast (see i.e., Harr *et al.*, 1983). Identical nonlinear normal mode initialization was used for the two models. As mentioned in the Introduction the purpose of the study is to evaluate the performances of the two models in comparison with observation and identify the causes of deficiencies by comparing the errors in the two models. Here we have estimated the systematic errors in the two models and also estimated the statistical significance of the systematic errors so that we consider the significant error for identifying the causes.

Let x_f and x_o represent the forecast and analysis field at the verifying time respectively. Hence the error field of the variable is

$$x = x_f - x_o. \tag{1}$$

If we have m forecasts corresponding to m initial values coming from fairly uniform climatic conditions. The ensemble error field is, $\bar{x} = \frac{1}{m} \Sigma x$ where, m = 9.

$\bar{x}$ is then the ensemble mean of error or the systematic error. The forecast field x *for any starting date* can be expressed as,

$$x = \bar{x} + x' \tag{2}$$

where x′ is the transient error. The total mean square error,

$$\frac{1}{m} \Sigma x^2 = \bar{x}^2 + \frac{1}{m} \Sigma (x')^2, \tag{3}$$

is the sum of square of the systematic error and the mean square transient error. The zonal average of the error field is,

$$x_z = \frac{1}{2\pi} \int_0^{2\pi} x \, d\lambda \qquad (4)$$

where λ is the longitude. An average of x_z over a latitude belt between ϕ_1 and ϕ_2 is,

$$\tilde{x} = \frac{\int_{\phi_1}^{\phi_2} x_z \cos\phi \, d\phi}{\int_{\phi_1}^{\phi_2} \cos\phi \, d\phi} \qquad (5)$$

In order to determine the significance of the systematic error we have computed the students "t" statistic assuming that the forecast and observed variables are independent and normally distributed with the same population variance as:

$$t = \frac{\tilde{x}}{\sqrt{v + v_0}} \sqrt{m-1} \qquad (5)$$

where, $v = \frac{1}{m} \Sigma(x_f - \bar{x}_f)^2$, $v_0 = \frac{1}{m} \Sigma(x_0 - \bar{x}_0)^2$

and $\bar{x}_0 = \frac{1}{m} \Sigma x_0$, mean of the analysis.

The t–values can be tested with a pre–selected level of significance. The t–value computed has (2m–2) or 16 degrees of freedom assuming that the forecast error is normally distributed at each grid point and the nine cases selected are statistically independent. If the t–values lie outside the range ±2·1 would imply that the systematic error is significantly different from zero at a grid point for a two–tailed test at the 95% level. However, one has to be careful in interpreting the significance of this test. First, all nine cases may not be statistically independent, second this test is valid only at a grid point and not for a field. Because x is highly correlated with neighboring grid points more

sophisticated tests have to be employed for field significance (Livezy and Chen, 1983). The "t" test used here may still be used as a guidance rather than an accurate measure of statistical field significance.

4.   RESULTS

We shall begin with a comparison of root mean square errors in the 500 mb geopotential height forecasts with the AFGL and COLA models. Figure 1 shows systematic, transient and total errors in day–1 through day–10 forecasts averaged over $22°$ N–$86°$ N region for the two models. The error levels and error growth rates of systematic, transient and total errors in the two models are strikingly similar. The error growth rate for the first seven days is larger than that for the last three–day period. Most likely the error in some spatial scales is saturated by day 7. The systematic error which is less than 20m for day 1 forecast grows to about 70m by day 10. The systematic error is almost half as much as the total error. This provides significant room for improving the forecast if the systematic errors are entirely due to the approximations in simulating dynamical and physical processes. The errors in 500 mb geopotential height for day 1 to day 10 forecasts averaged over the tropical belt, $22°$ N–$22°$ S are shown in Figure 2. Here there is a significant difference between the systematic errors in the two models. The systematic errors for days 1 to 10 in the AFGL model is almost twice as much as in the COLA model. For day 10 the systematic error is about 33m in the COLA model whereas in the AFGL model it is close to 68m. The level of systematic errors for days 1 to 10 in tropics is about the same as in extra–tropics in the AFGL model. The transient error is about the same in the two models. In both models, the systematic error dominates the total error, in contrast to extra–tropics. Similar characteristics were noted in ECMWF forecast model (Heckley, 1985). In the tropics, error grows rapidly and saturates sooner than in extratropics (Shukla, 1981). The error growth rate for the first three days is larger than that for the remaining part of the forecast period.

11

500 mb height error (22N - 86N ave)

——————	cola sys err
———·——	afgl sys err
—·—·—·	cola trans err
—·—·—·	afgl trans err
— — —	cola total err
— — —	afgl total err

Origin At 1.00,0.0
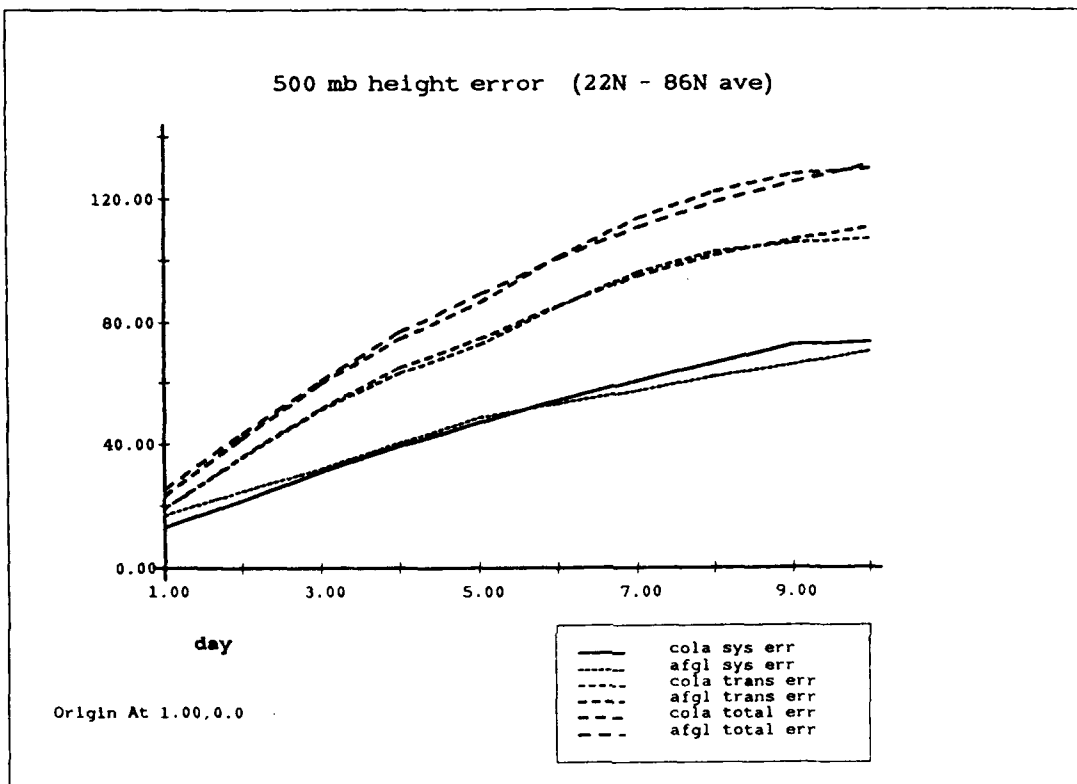
Figure 1   The time evolution of 500 mb geopotential height errors for AFGL and COLA
models averaged over extratropics (22° N–86° N) for ten days forecasts.
Units: m.

500 mb height error (22N - 22S ave)

Origin At 1.00,0.0

———	cola sys err
———	afgl sys err
-----	cola trans err
- - - -	afgl trans err
— — —	cola total err
— —.	afgl total err

Figure 2.   Same as Figure 1 except the errors are averaged over the tropical belt (22° N–22° S).

13

The geographical structure of systematic error of the 500 mb geopotential height for day 10 forecast is presented in Figure 3. The two models have similar error structures in that they are negative in the tropics and positive in the extratropics except over Arctic ocean north of Eurasia. These general characteristics are also common to other models: NMC (Kanamitsu et al., 1990), GFDL (Sirutis and Miyakoda, 1990) and ECMWF (Heckley, 1985). The error character is dominated by zonal wave number four in midlatitudes and zonal wave number one in high latitudes. The phas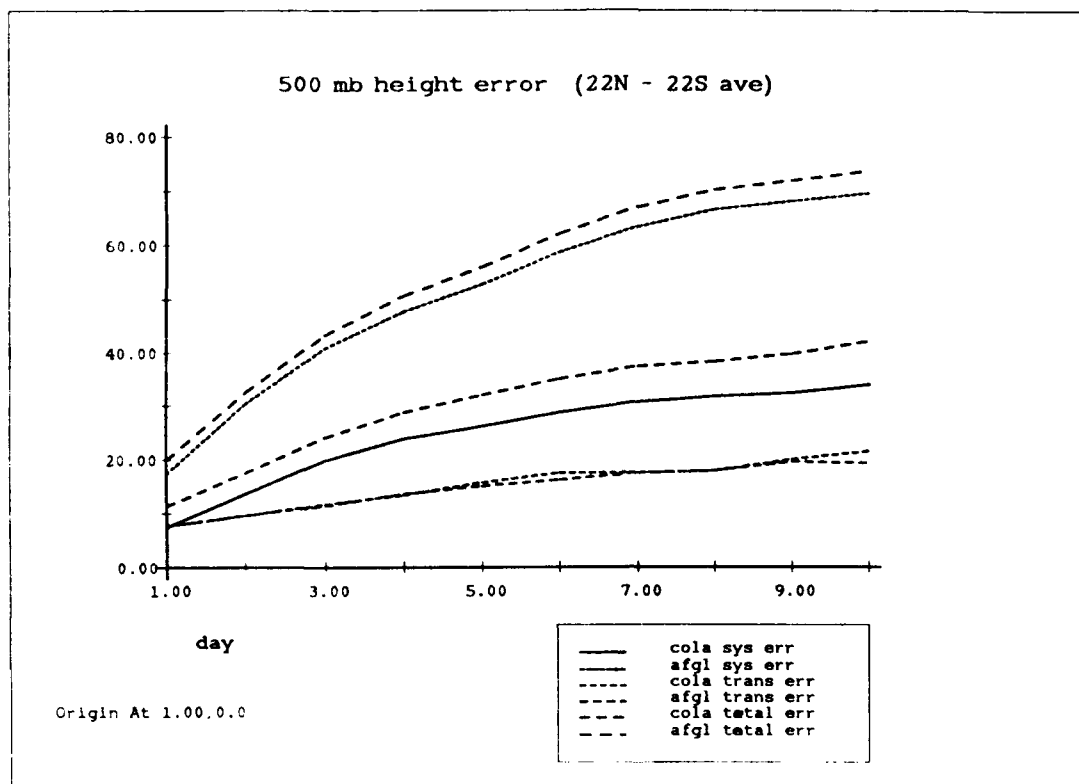e and amplitude of the error fields of the two models are similar with minor exceptions. The magnitude of negative errors around 45°N and 45°S in the COLA model are larger than those for the AFGL model. Large tropical errors in the AFGL model seen in Figure 2 are apparent in Figure 3. An 80m isopleth covers a large monsoon region over Indonesia, Borneo, Philippines, Southern Brazil and the Atlantic Ocean. A 60m isopleth covers a very large part of the tropics. Whereas in the COLA model 40m isopleth covers a large region of tropics. The errors in tropics can be a serious problem for the predictability of extratropics flow beyond 10 days because the errors from tropics propagate and contaminate the predictions in extratropics (see, Palmer et al., 1990). The geographical distribution of the transient error in day 10 for the two models is shown in Figure 4. The transient error patterns in the two models are very similar. The error level in extratropics is an order of magnitude larger than in tropics. Comparing the extratropical transient error pattern with that of systematic error in Figure 3 we find the level of transient error is large where absolute magnitude of systematic error is large. This characteristic is also common to other models, ECMWF and GFDL (see, Hollingsworth et al., 1980). The total error for day 10 is shown in Figure 5. It reflects the combination of error structures seen in Figures 3 and 4.

Finally the distribution of t-values for day 10, which is a measure of significance of the systematic error is, shown in Figure 6. The systematic error may be considered significantly different from zero in a region where absolute value of t exceeds 2.1. As noted

14

Figure 3.   The systematic errors in 500 mb geopotential height for day 10 forecast. Upper panel is for AFGL model and lower panel is for COLA model. Contour interval is 20 m.

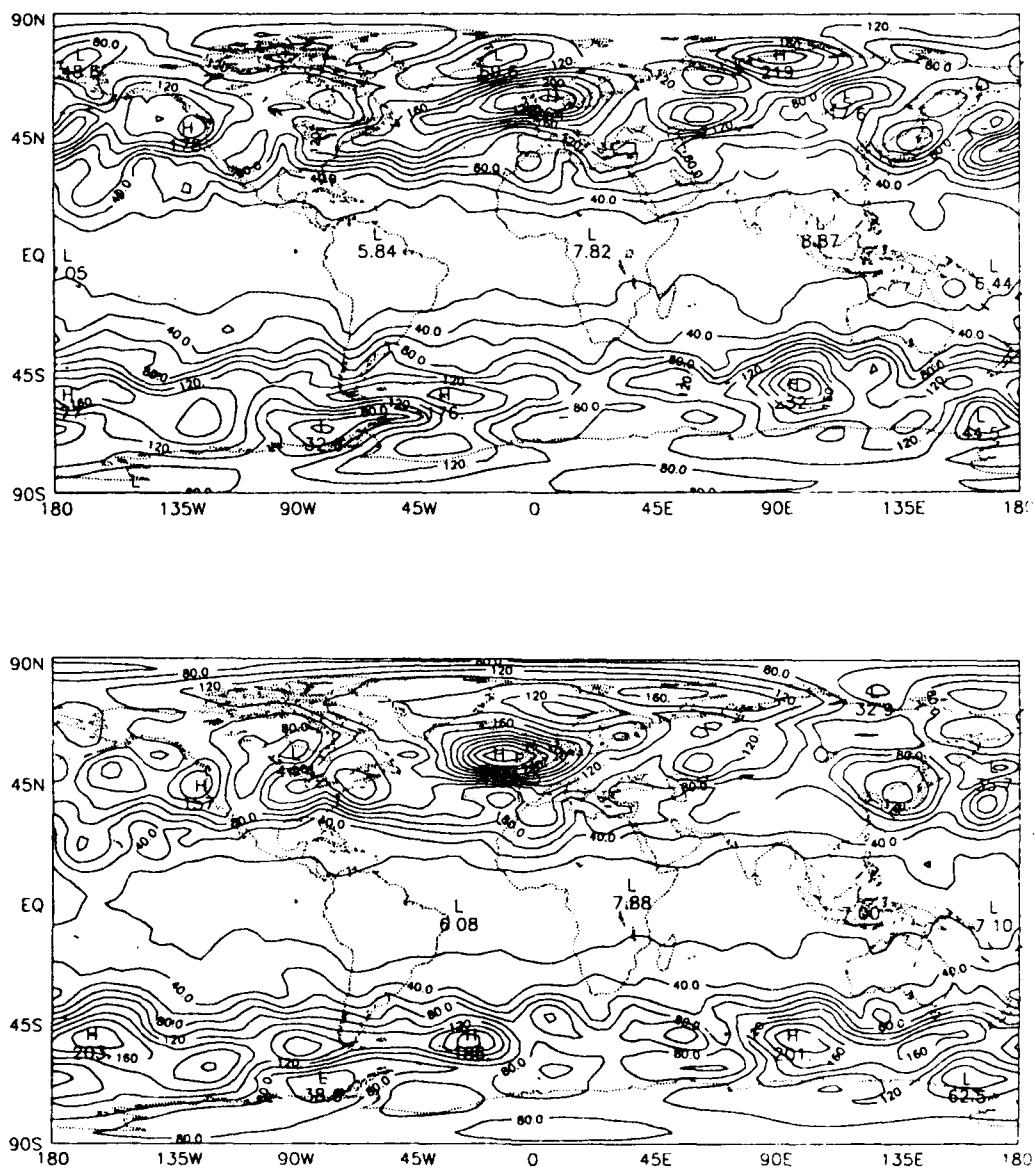Figure 4. Same as Figure 3 except the transient errors.

Figure 5   Same as Figure 3 except the total errors.
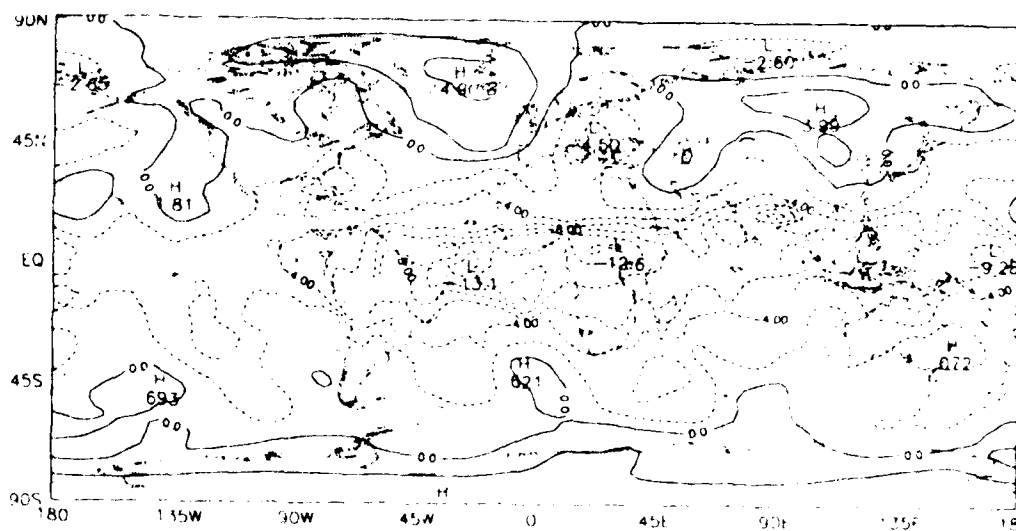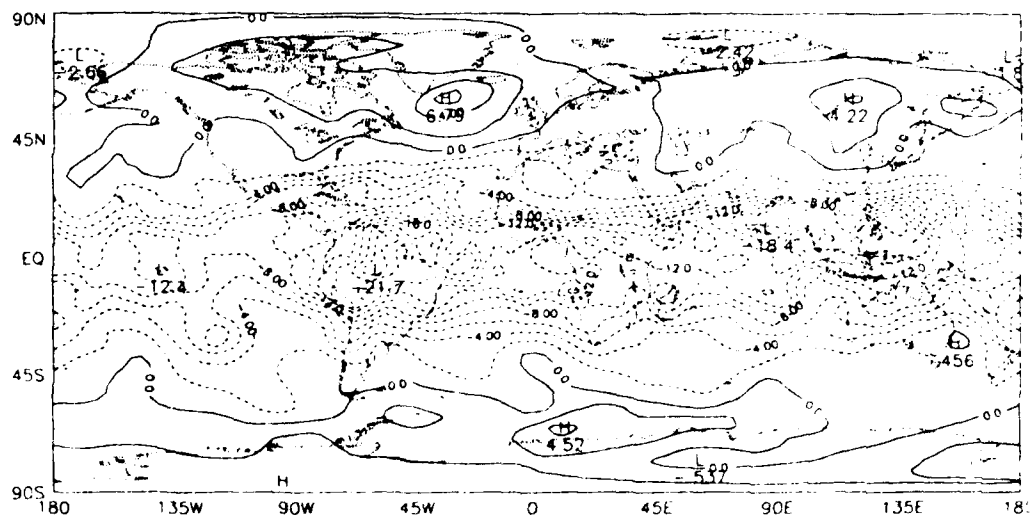
Figure 6.   Same as Figure 3 except t-values   Contour interval is 2

earlier, this is not an accurate test of field significance, therefore we should interpret the results with some caution. Both models show similar characteristics, that is, the systematic error in the tropics is significantly different from zero whereas for large regions of extratropics they are not. There are some regions over North Atlantic ocean and Siberia where the systematic errors are probably different from zero. In tropics, the level of significance is higher for the AFGL model compared to that for the COLA model.

Next we shall examine global error statistics for 850 mb temperature averaged over 22°N-86°N region shown in Figure 7. The general characteristics of systematic, transient and total errors for the two models are very similar to those for the 500 mb geopotential height in Figure 1. The levels and growth rate of errors in the two models are about the same. The level of systematic error in the two models is about 1.5°K for day 1 and by day 10 it is about 3.4°K. The systematic error for the first two days of the forecast is larger than the transient error. As in the case of 500 mb geopotential height error, the rate of error growth in 850 mb temperature for the first seven days is larger than that for the remaining part of the forecast period.

The 850 mb temperature error statistics for the tropical belt between 22°N and 22°S are shown in Figure 8. The transient error level in the two models are about the same, slightly lower than 1°K for day 1 and slightly higher than 1°K for 10 day. The systematic errors in the two models differ significantly. For day 1 the systematic error it is about 2.8°K in the COLA model and 3.4°K in the AFGL model. For day 10 it is about 3.8°K in the COLA model whereas it is about 5.2°K in the AFGL model. The error growth rate of systematic error is large for the first two days of forecast. By day 4 it appears that the error is probably saturated in most of the spatial scales. The error characteristics in 850 mb temperature are similar to those in 500 mb geopotential height field. This is more clearly seen in Figure 9 which shows the geographical pattern of the systematic errors for the two models. There are negative errors in the tropics and positive errors in extratropics

850 mb temp. err   (22N - 86N ave)

Origin At 1.00,0.0

——	cola sys err
--------	afgl sys err
------	cola trans err
----	afgl trans err
— —	cola total err
— — -	afgl total err
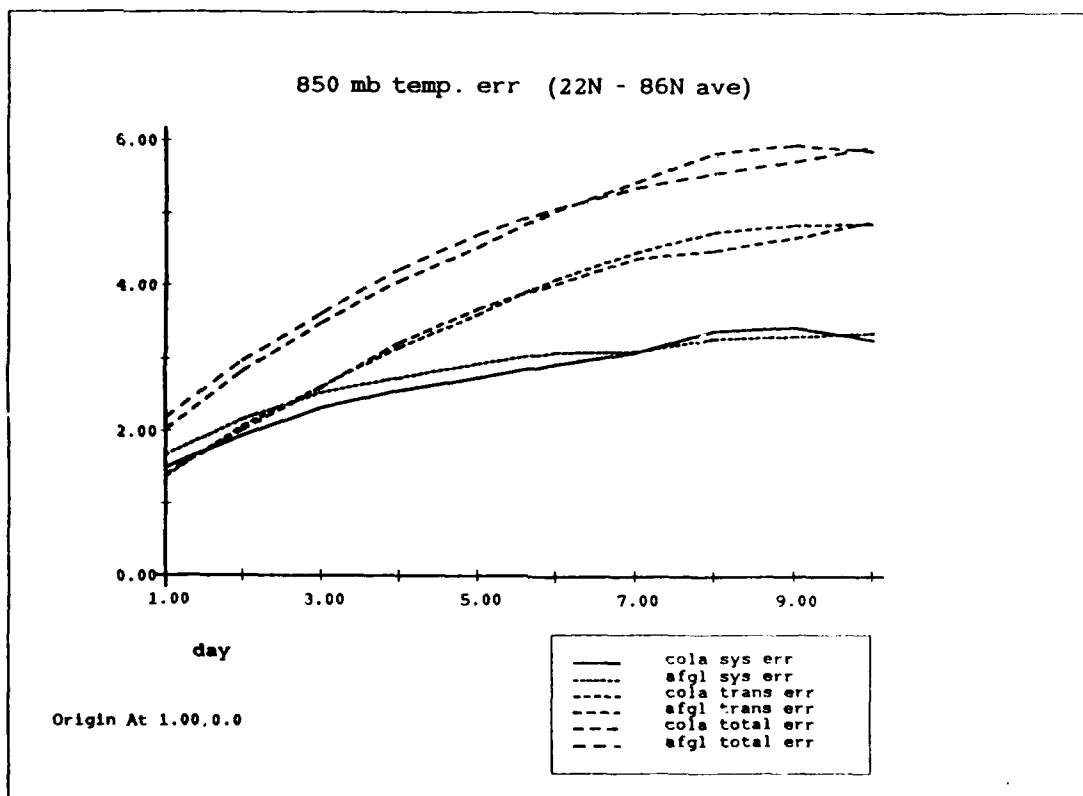
Figure 7   The time evolution of 850 mb temperature error for AFGL and COLA
models averaged over extratropics, (22° N–86° N). Units: °K.

20

850 mb temp. err (22S - 22N ave)

Origin At 1.00,0.0

————	cola sys err
———	cola trans err
- - - - -	cola total err
- - - -	afgl sys err
— — —	afgl trans err
— — ·	afgl total err

Figure 8.   Same as Figure 7 except the errors are averaged over the tropical belt (22° N–22° S)
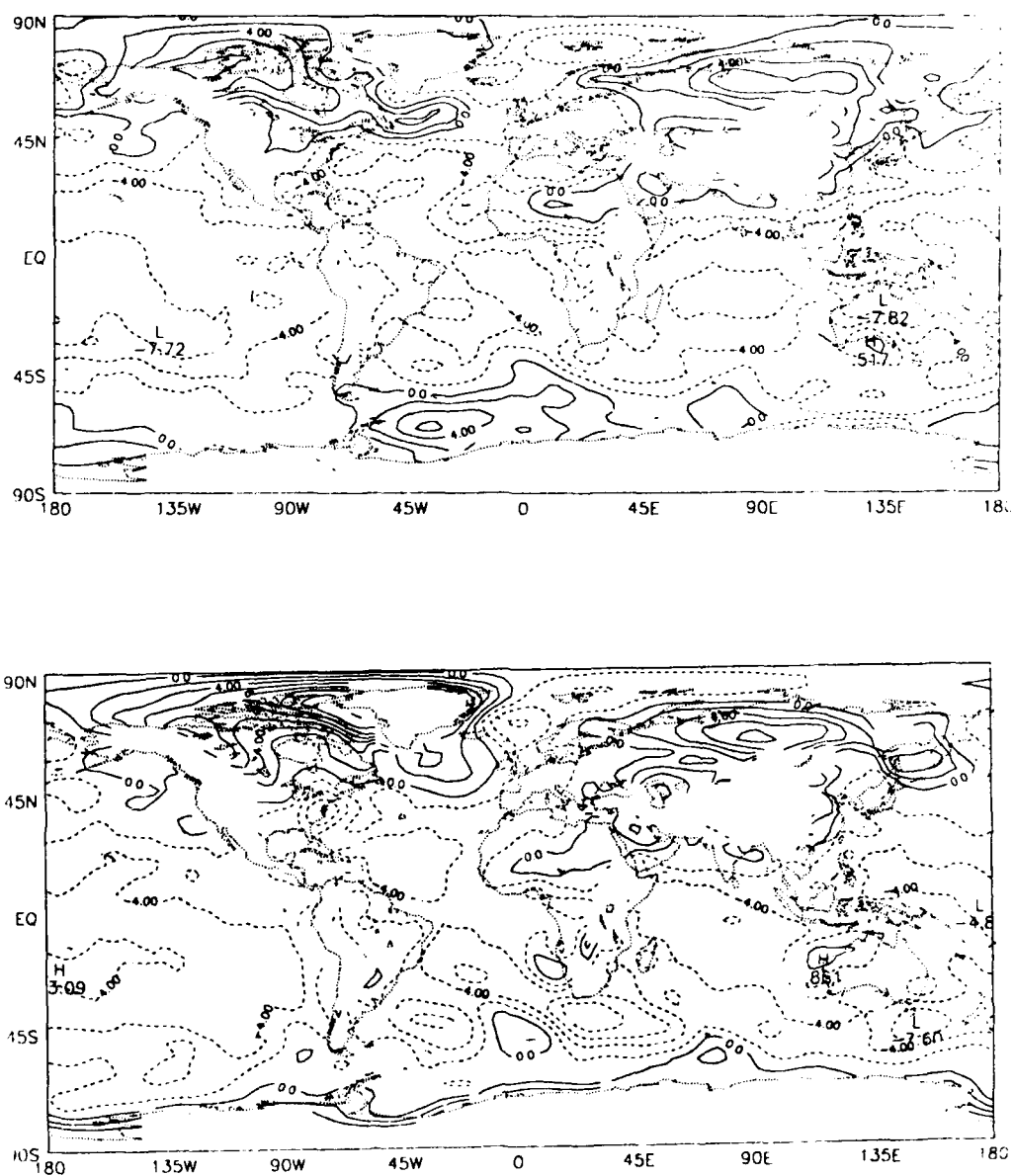
Figure 9. The systematic errors in 850 mb temperature for day 10 forecast. Upper panel is for AFGL model and lower panel is for COLA model. Contour interval is 2° K.
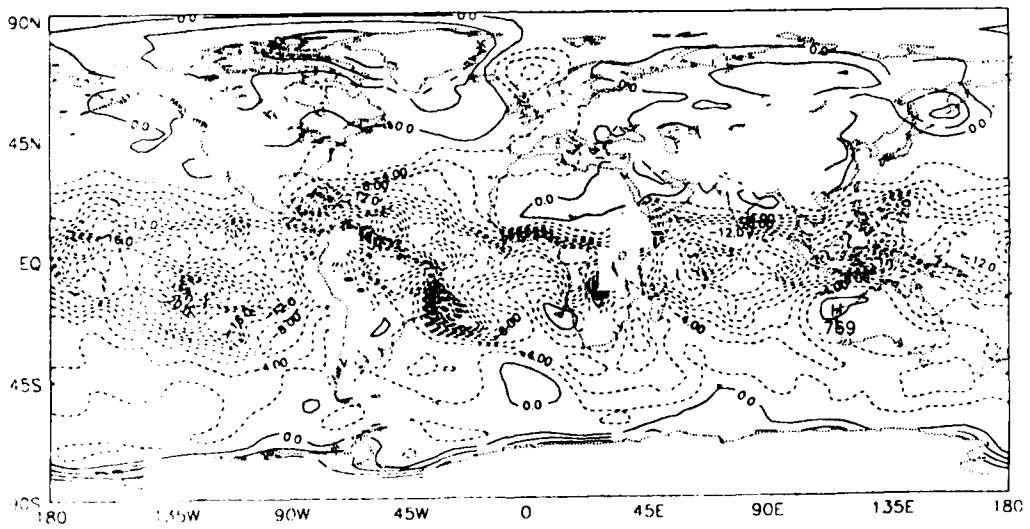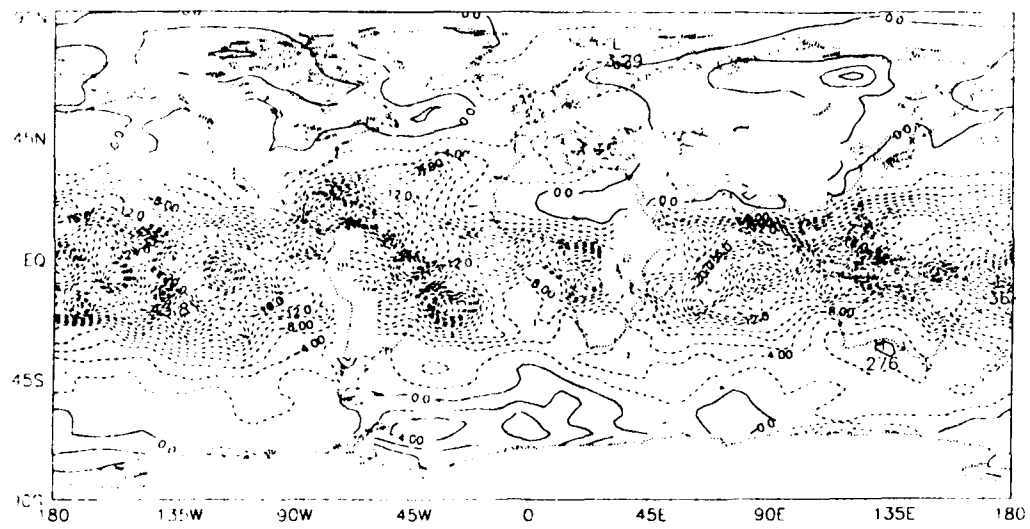
Figure 10.   Same as Figure 9 except for t-values.

except over Arctic Ocean north of Eurasia. However there is a difference in the error structure between 850 mb temperature and 500 mb geopotential height, that is, the magnitude of error in tropics and extratropics. The magnitude of 850 mb temperature error in tropics is about the same as in extratropics except in Northern Territories of Canada which differ from that of 500 mb height field. A 4°K isotherm covers a large region of tropical oceans in both the models but in the AFGL model forecast there are large regions of 6°K isotherms over the Pacific and Indian Oceans and a small region over the Atlantic Ocean.

Similarities in Figure 3, the 500 mb geopotential systematic error and Figure 9, the 850 mb temperature systematic error, are expected because of the hydrostatic relation. The general pattern of these two figures, that is, cold in tropics and warm in extratropics suggest that the baroclinic properties of the models are going to differ from that of the atmosphere because of weaker north–south temperature gradient. Some of the error structure in the extratropics in Figure 3 may be a consequence of growth rate and propagation speed of some waves in the model differing from those of the atmosphere (Lambert and Merilees 1978). Again this characteristic is also common to other forecast models and GCMs (Kanamitsu *et al* 1990; Heckley 1985; Sirutis and Miyakoda 1990). The significance of 850 mb temperature systematic error pattern is shown in Figure 10. The errors in tropics appear highly significant in both the models. There are also some regions in extratropics such as over Siberia, Greenland and North Atlantic Ocean where the errors are probably different from zero.

The errors in the 850 mb relative humidity averaged over the globe (86°N–86°S) for the two models is shown in Figure 11. The systematic error in the COLA model is slightly lower than that in the AFGL model for the two days forecast but then it increases and by day 10 it is about 2% higher than that in the AFGL model. The transient error in AFGL model is larger than that in the COLA model and as a result the total error in the AFGL

850 mb rel humidity (86S - 86N ave)

Origin At 1.00,0.0

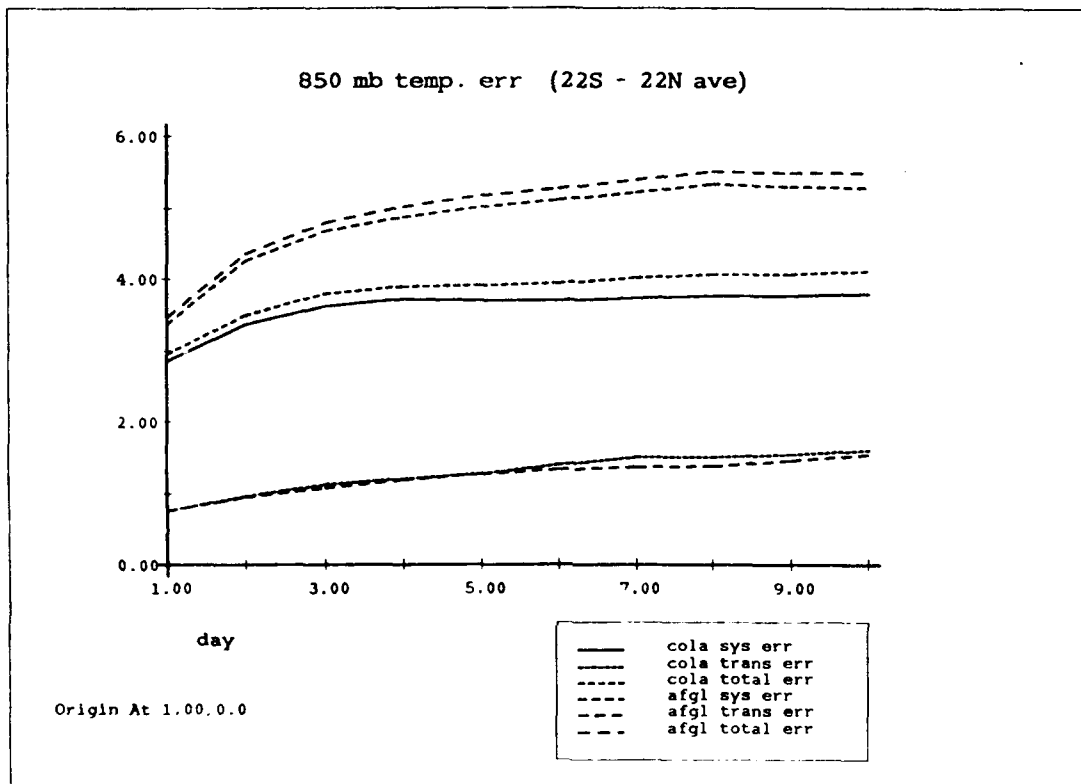|	
——	cola sys err
·———	cola trans err
——··	cola total err
———·	afgl sys err
———	afgl trans err
—·—··	afgl total err

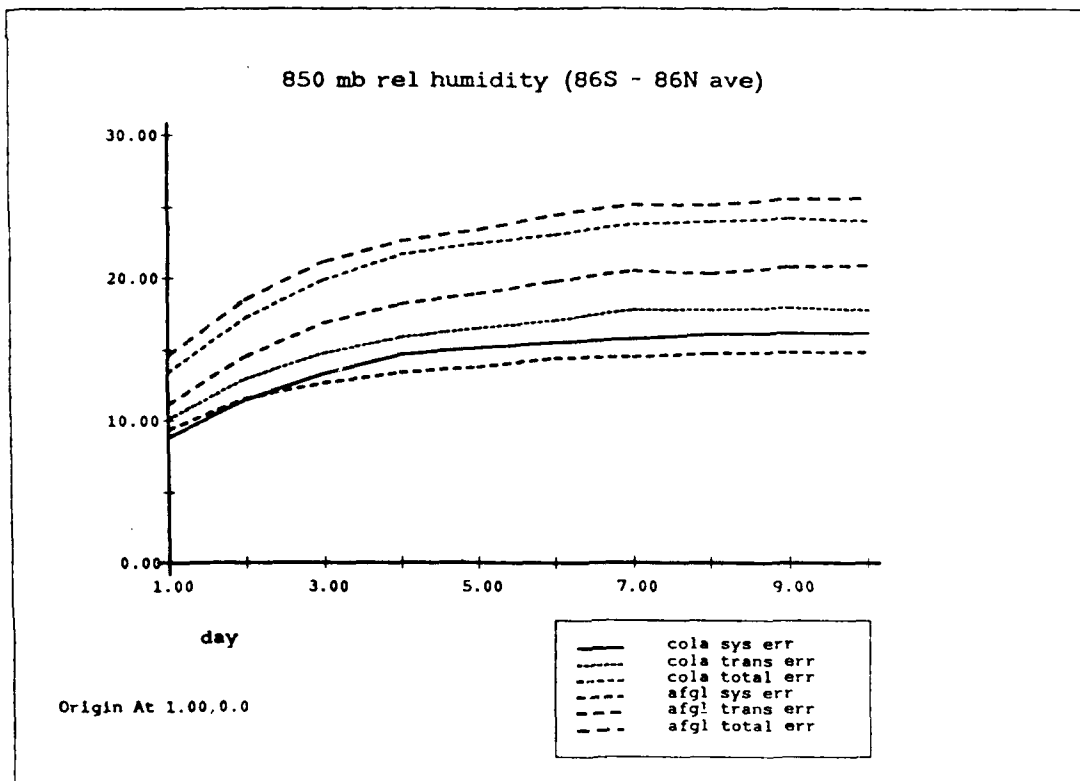Figure 11.   The time evolution of 850 mb relative humidity errors in per cent for AFGL and COLA models averaged over the globe (86° S–86° N).
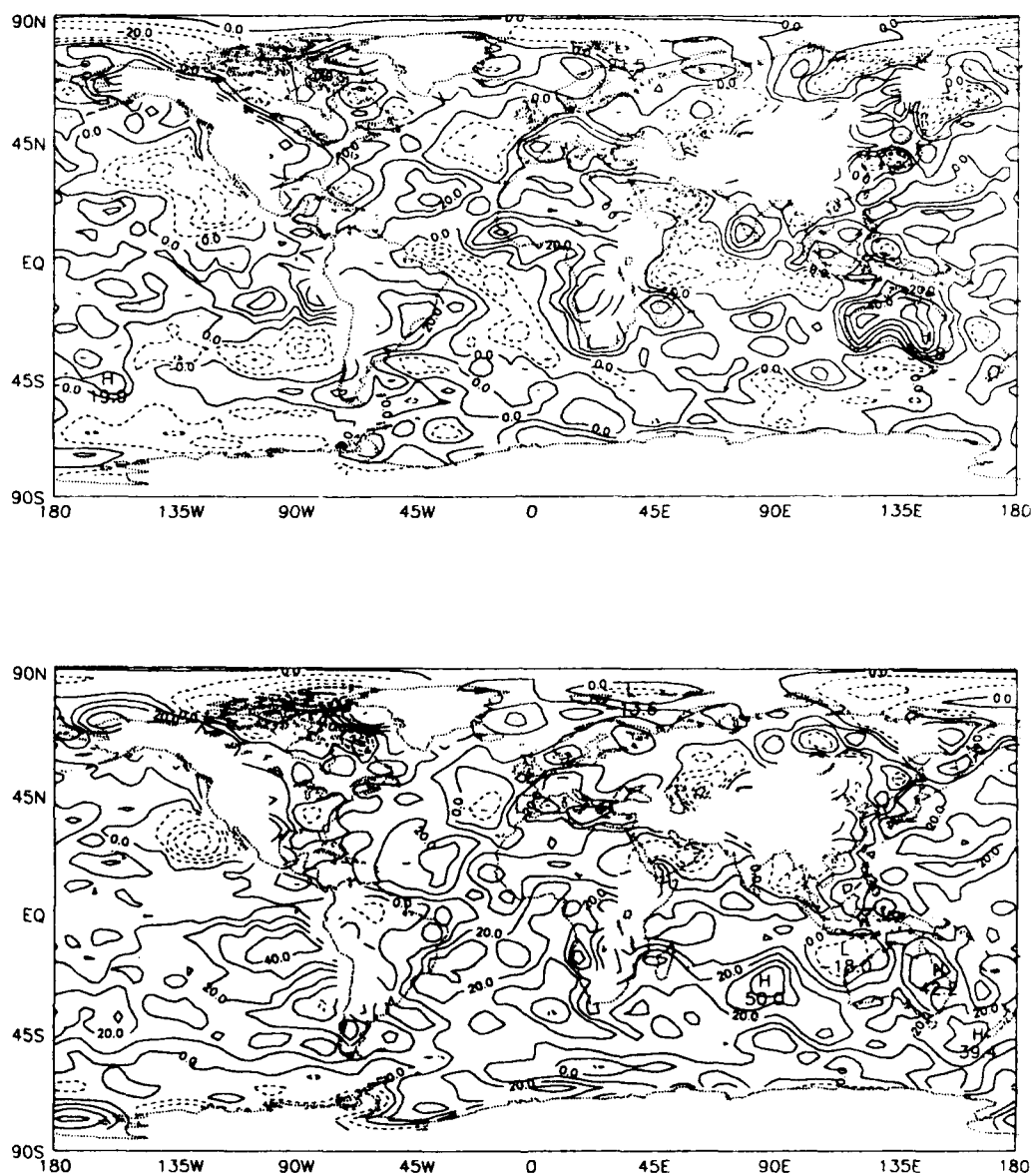
25

Figure 12. The systematic errors in 850 mb relative humidity for day 10 forecast. Upper panel is for AFGL model and the lower panel is for COLA model. Contour interval is 10%.

Figure 13.   Same as Figure 12 except for t-values. Contour interval is 2.

model is larger than that in the COLA model. The error growth rate is much higher for the first four days of forecast compared to the remaining period which is characteristic of error growth in the tropics. Geographical distributions of the systematic errors for day 10 in the two models are shown in Figure 12. In the AFGL model, negative errors are largely over the oceans. The regions of negative errors are over the north and southeastern part of the Pacific Ocean, south and north of the eastern part of Atlantic Ocean, and equatorial Indian Ocean. Over land, errors are largely positive except for small regions over eastern Europe, northeastern Siberia and Northern Territories in Canada. In the COLA model, the errors are mostly positive except small regions over the Pacific Ocean west of California, northwestern Brazil, eastern Soviet Union, Saudi Arabia and in the Indian Ocean south of Indonesia. If the relative humidity errors are largely due to errors in the 850 mb temperature one would expect mostly positive errors in the tropics and negative errors in the extratropics because the saturation vapor pressure decreases with decreasing temperature. In the COLA model the temperature errors may be responsible for the relative humidity errors to some extent. The errors in the AFGL model may be caused by the fact that the vertical flux of moisture over oceans is not properly simulated by the boundary layer physics or by the shallow convection. A comparison of tropical relative humidity errors in the two models suggests that the AFGL model is drier than the COLA model whereas the former is colder in tropics than the latter. Hence the specific humidity negative errors in the AFGL model are probably larger because the saturation vapor pressure decreases with temperature.

Errors in relative humidity or specific humidity can have serious consequences on prediction beyond 10 days because of their influence on other physical processes such as cloud–radiation interaction and precipitation. The drier atmosphere (or negative specific humidity error) is less opaque to the infrared radiation and as a result it will cool further. Supersaturation clouds are simulated from model generated relative humidity. Positive

relative humidity errors are likely to generate more clouds. Assuming that the albedo effect (cooling) of clouds dominates the greenhouse effect (warming), more clouds will cool the atmosphere. Whereas the negative relative humidity errors will warm the atmosphere. The moisture convergence and conditional instability are necessary conditions for convective precipitation. Precipitation due to supersaturation is determined from the relative humidity. The errors in relative humidity (specific humidity) can affect the amount of precipitation and hence that of latent heat of condensation.

The t-values for the relative humidity are shown in Figure 13. The area of significant systematic errors in the AFGL model is less than that of the COLA model. The magnitudes of systematic errors in the AFGL model are slightly lower than those of the COLA model but at the same time the transient errors in the AFGL model are larger than those of the COLA model as seen in Figure 11.

The errors in 150 mb temperature averaged over extratropics 22° N–86° N, are shown in Figure 14. The systematic error in the AFGL model is about the same as that of the COLA model for the first two days of the forecast but then it decreases and by day 10 it is about 0.4° K less than that of the COLA model. However the transient error in the AFGL model is larger than that of the COLA model. The error growth rate characteristics of 150 mb temperature are similar to that of 850 mb temperature. The growth rate is larger for the first seven days compared to that of the remaining period. The geographical patterns of the systematic error in the two models are shown in Figure 15. Extratropical error patterns in the two models are similar. They are mostly negative except over northern Eurasia. The major differences are in the tropical error. In the AFGL model they are mostly positive and large. In the COLA model they are mostly negative with some positive error regions over India, Indian Ocean, south Atlantic Ocean and southeastern Pacific Ocean. The significance of 150 mb temperature error is shown in Figure 16. Tropical systematic errors in the AFGL model appear significantly different from zero whereas in the COLA model there are some regions where the error is not
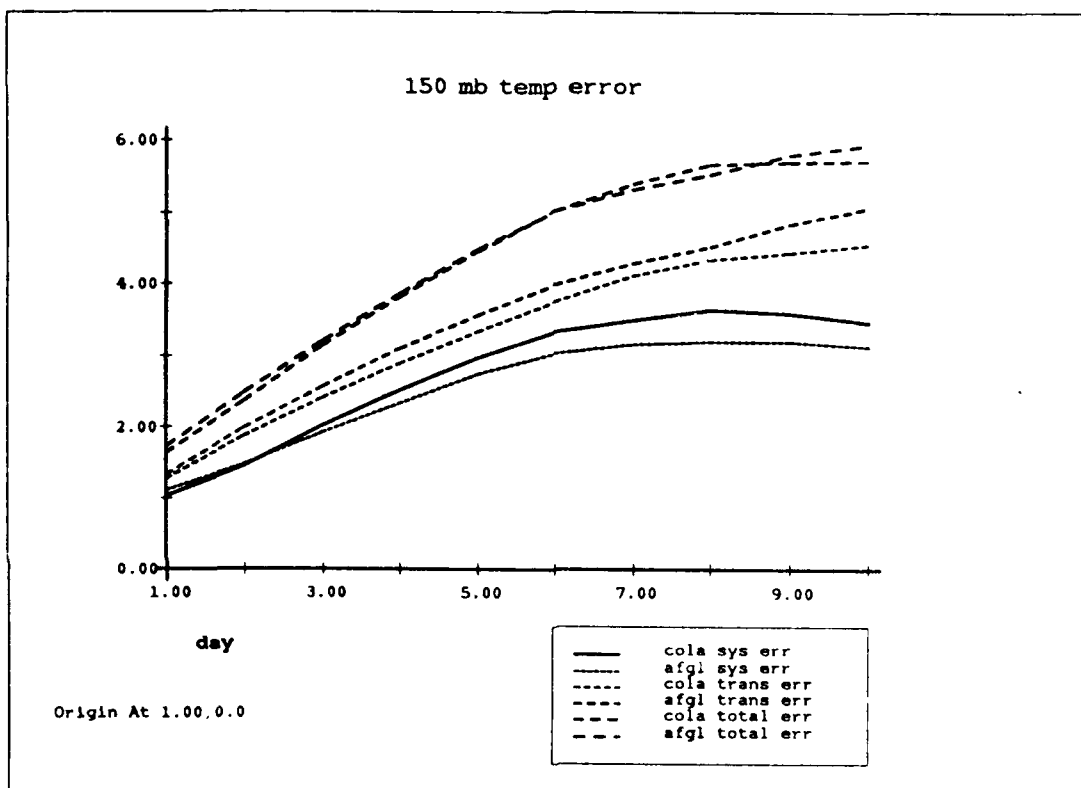
29

Figure 14   The time evolution of 150 mb temperature error for AFGL and COLA
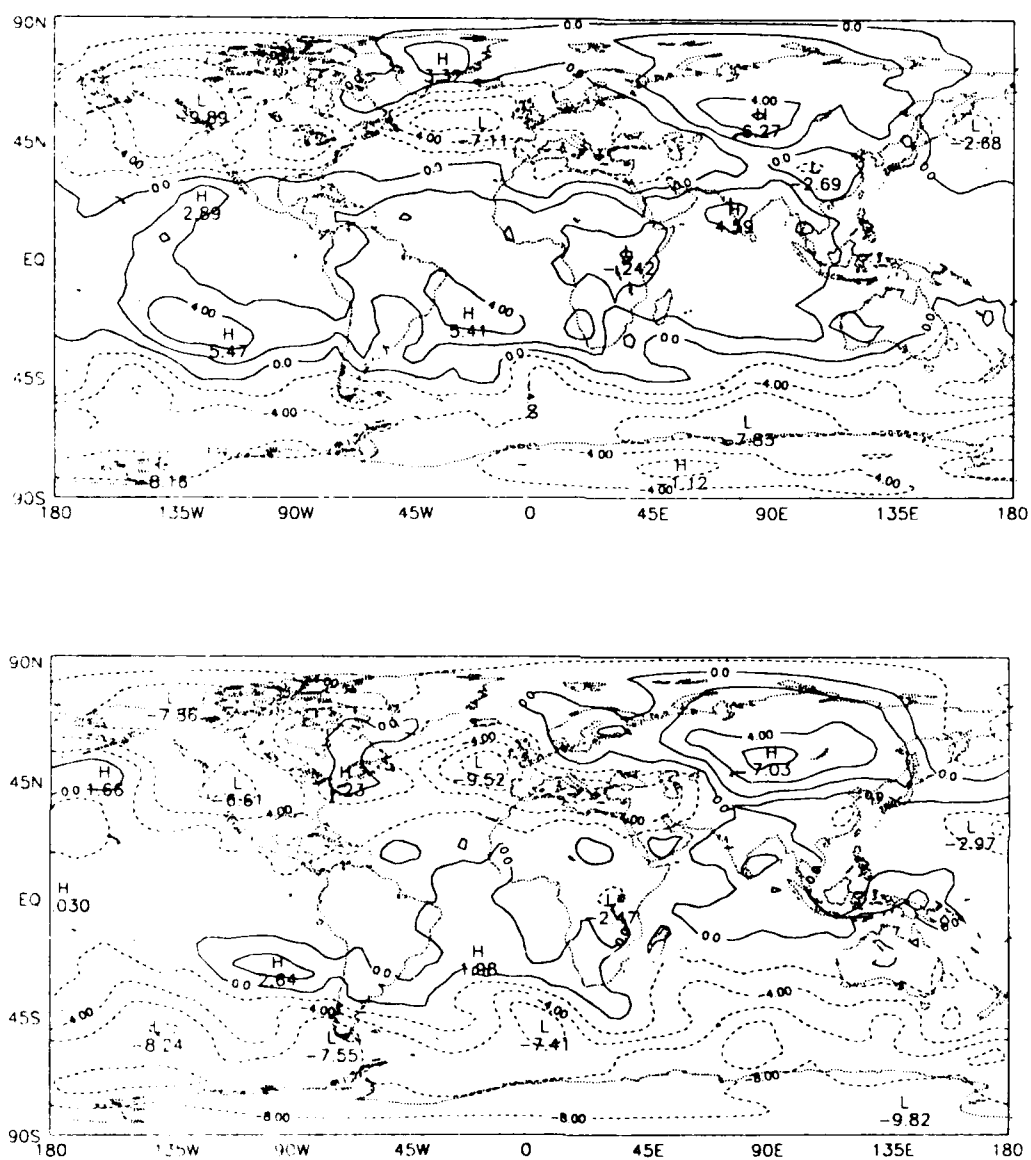models averaged over extratropics (22° N–86° N). Units: ° K.

Figure 15.   The systematic errors in 150 mb temperature for day 10 forecast. Upper panel is for AFGL model and lower panel is for COLA model. Contour interval is 2° K.
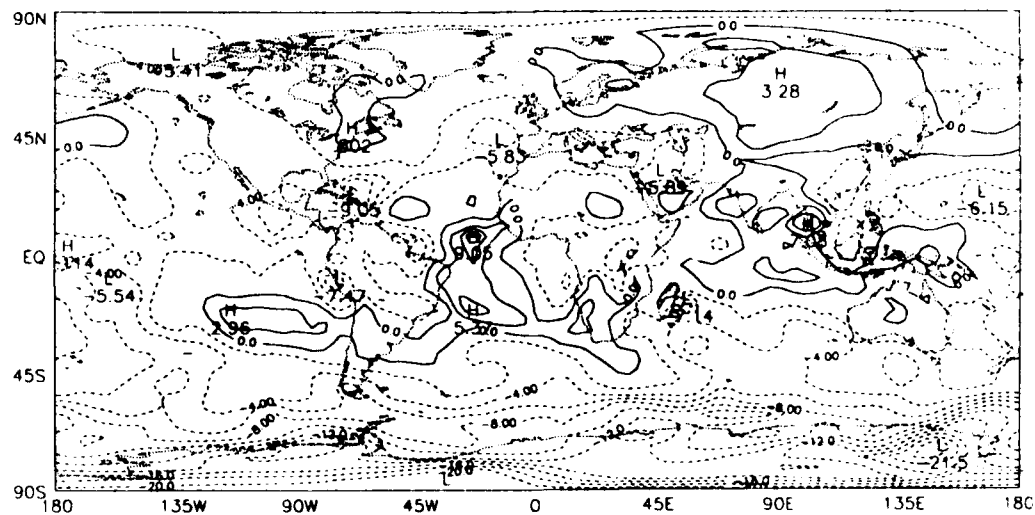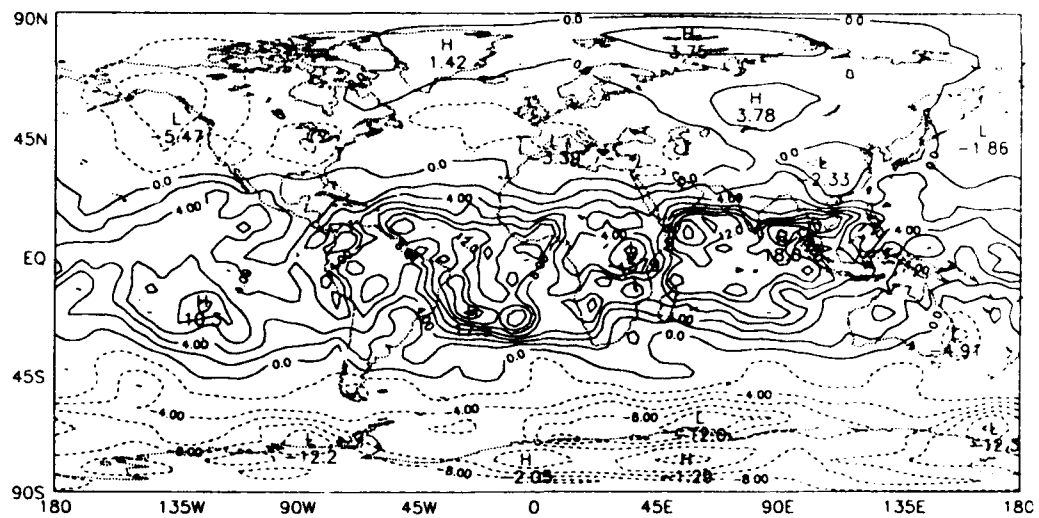
Figure 16.   Same as Figure 15 except for t-values. Contour interval is 2.

different from zero. In both the models errors in the southern hemisphere extratropics are significant. In the northern hemisphere extratropics there are only a few regions where the error is significant.

Now we shall consider the error structure and their statistical significance in zonally averaged temperature and zonal winds. The systematic errors of zonally averaged temperature for the AFGL and COLA day 10 forecasts are shown respectively in Figures 17a and Fig. 17b. Both models have similar error structure in that the troposphere is cold except in high latitudes of lower troposphere and equatorial lower stratosphere. The only major difference in the two figures is the magnitude of tropical stratospheric error which is larger in the AFGL model than in the COLA model. The characteristics of error structure in 850 mb temperature in Figure 9 that cold tropics and warm extratropics can be seen in the zonally averaged error field. As mentioned earlier, such error structure will reduce the baroclinicity of the model atmosphere. The vertical error structure, cold in lower troposphere and warm in lower stratosphere will reduce the convective instability of the tropical model atmosphere. However, these characteristics are not only common to these two models but also in other forecast and GCM models (Kanamitsu *et al.*, 1990; Sirutis and Miyakoda, 1990; and Heckley, 1985). As shown by the distributions of student's "t" statistic in Figures 18a and 18b, these systematic errors are statistically significant.

The systematic error in zonally averaged zonal wind for the AFGL and COLA models is shown in Figures 19a and 19b respectively. The error structures in the two models are similar in that the errors have a barotropic structure. Both models have easterly bias in tropics and westerly bias in southern hemispheric subtropics and again easterly bias in high latitude of the southern hemisphere. Both models have positive errors in high latitudes of the northern hemisphere and negative errors around 45°N. The COLA model has westerly bias in subtropics of the northern hemisphere but in the AFGL model they are only in the stratosphere and in the troposphere it has an easterly bias. Prior to
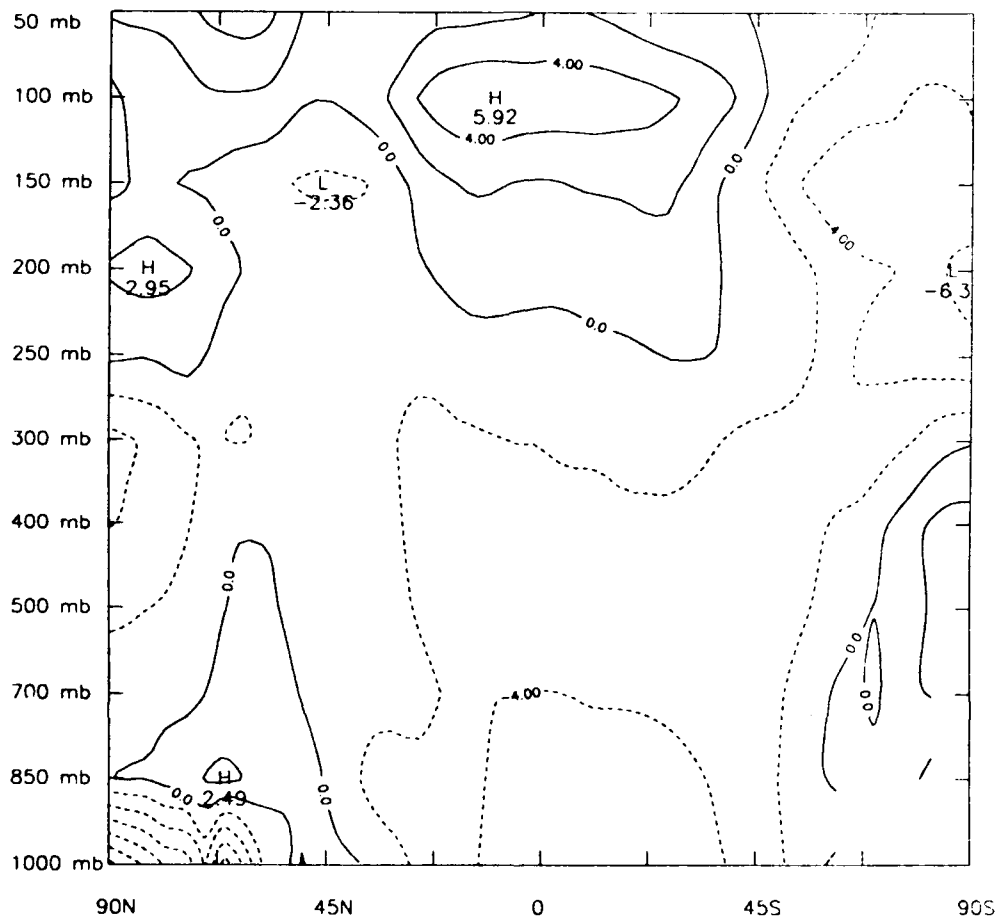
33

Figure 17a. The systematic errors in zonally averaged temperature for day 10 forecast with AFGL model. Contour interval is 2° K.
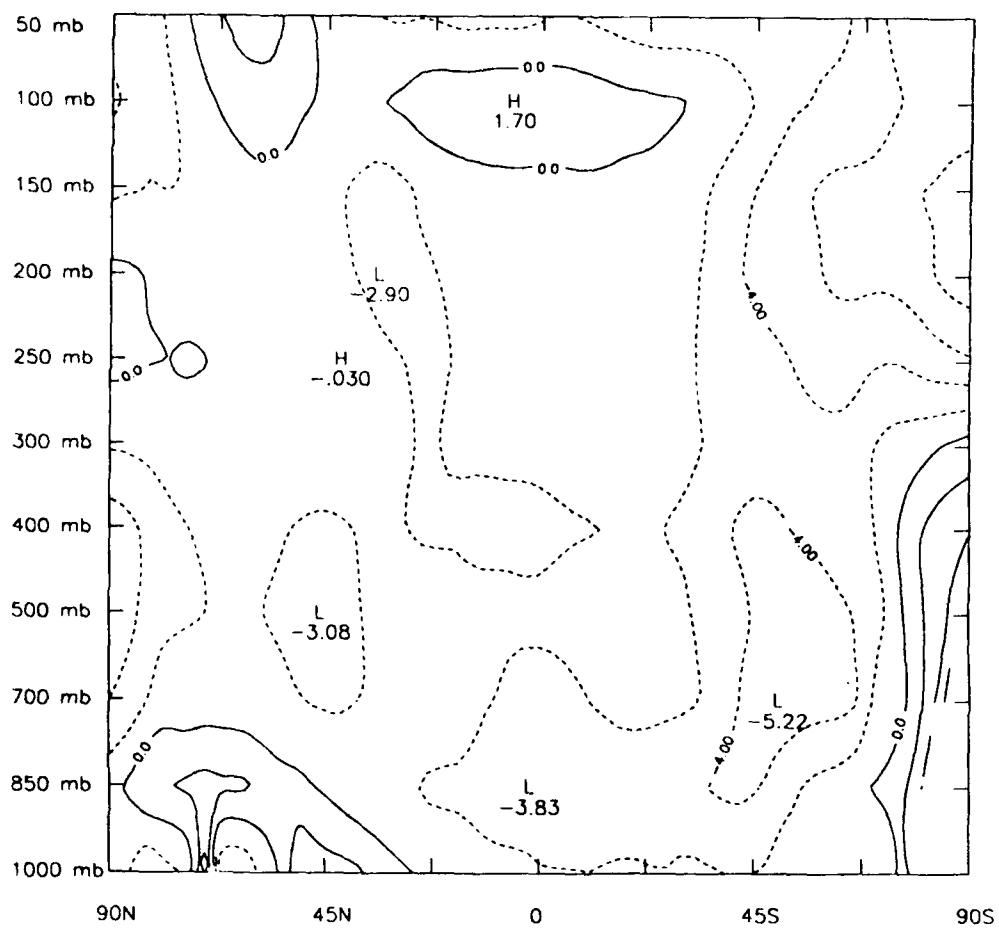
34

Figure 17b.   Same as Figure 17a except for COLA model.

Figure 18a. Same as Figure 17a except for t–values. Contour interval is 2.

Figure 18b.   Same as Figure 17b except for t-values. Contour interval is 2.

37

the inclusion of explicit parameterization of gravity wave drag the magnitude of these errors were much larger (see, Kirtman, *et al* 1991). The error structure of the zonal winds are consistent with errors in the zonally averaged temperature in that they approximately satisfy the thermal wind equation. Finally, the structure of the t–values for the AFGL and COLA models are respectively shown in Figures 20a and 20b. The major feature of the error structure is significant. However there are regions in the vicinity of zero isopleth the errors are not statistically significant.

5. SUMMARY AND CONCLUSIONS

We have made nine ten–day forecasts with the two models, AFGL and COLA, to study the systematic errors with the intent of identifying the sources of these errors. Nine initial dates were chosen from January 1990 such that they are synoptically independent. The geographical patterns of systematic errors and their statistical significance are computed for 500 mb geopotential height field, 850 mb temperature and relative humidity and 150 mb temperature. Additionally, vertical and meridional distributions of systematic errors and their statistical significance were computed for zonally averaged temperature and zonal wind. The systematic errors in the two models have some common features. For example, the errors in 500 mb geopotential height are negative in tropics and positive in extratropics. Consistent with 500 mb height errors, the 850 mb temperatures are cold in tropics and warm in extratropics compared to NMC analysis. The zonally averaged temperatures in tropics are cold in the troposphere and warm in the lower stratosphere. In the extratropics the temperatures are warm in lower troposphere and cold in the upper troposphere compared to the observations. The systematic errors of zonally averaged zonal winds have a barotropic character. By and large, the errors are negative (easterly bias) in the tropics, middle latitudes and high latitudes of the southern hemisphere. The positive errors (westerly bias) appear in the subtropics and high latitudes of the northern

38

Figure 19a.   The systematic errors in zonally averaged zonal wind for day 10 forecast
with AFGL model. Contour interval is 2 m/sec.
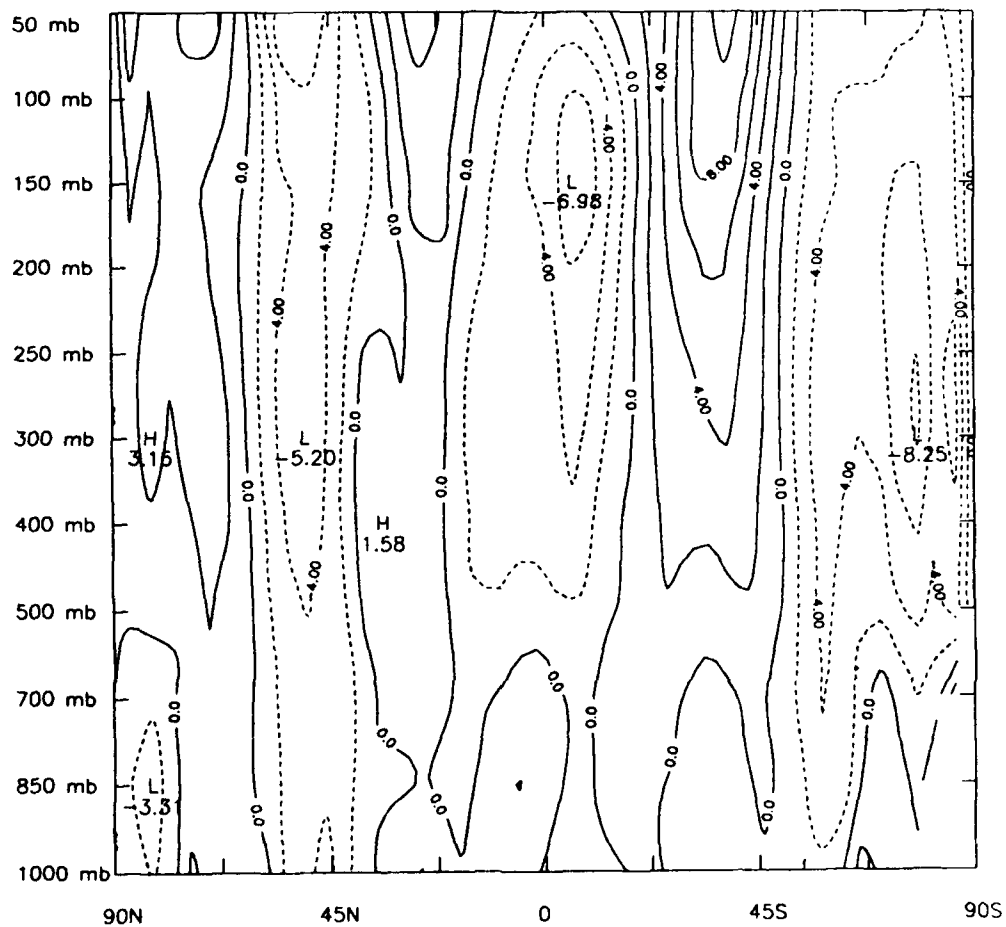
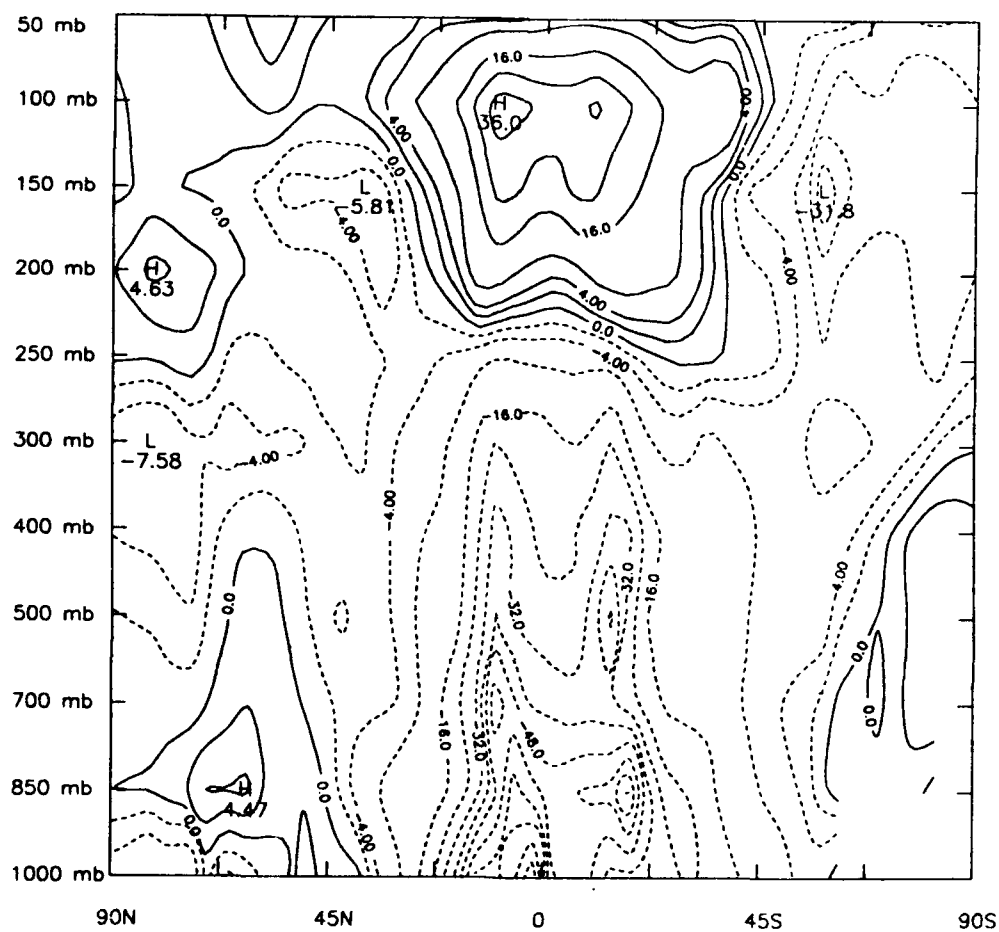**Figure 19b.** Same as Figure 19a except for COLA model.
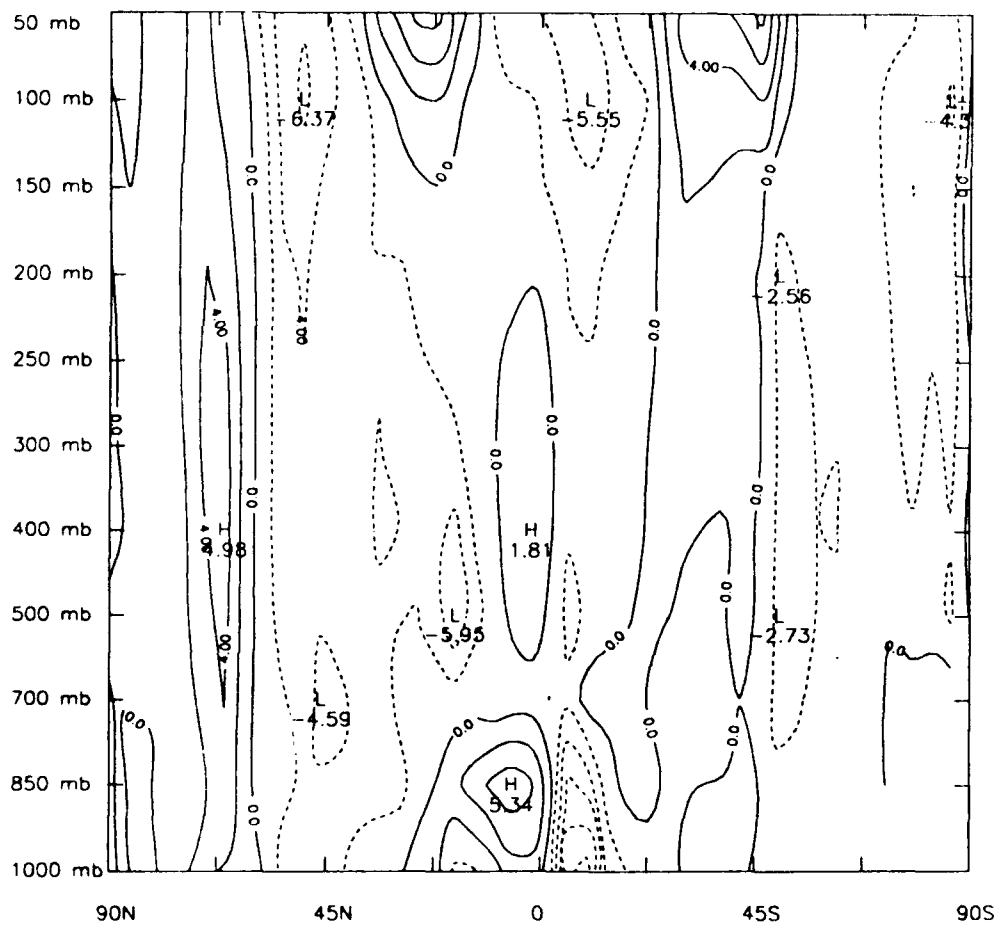
Figure 20a.   Same as Figure 19a except for t–values. Contour interval is 2.
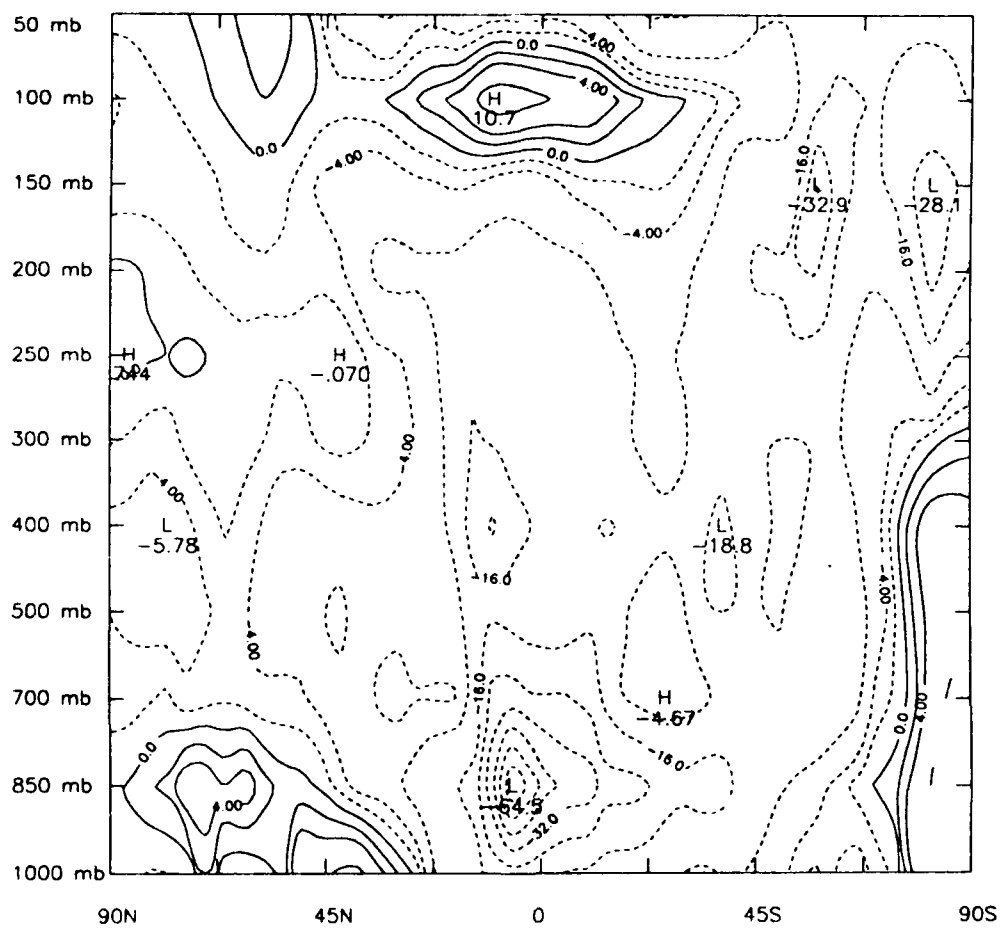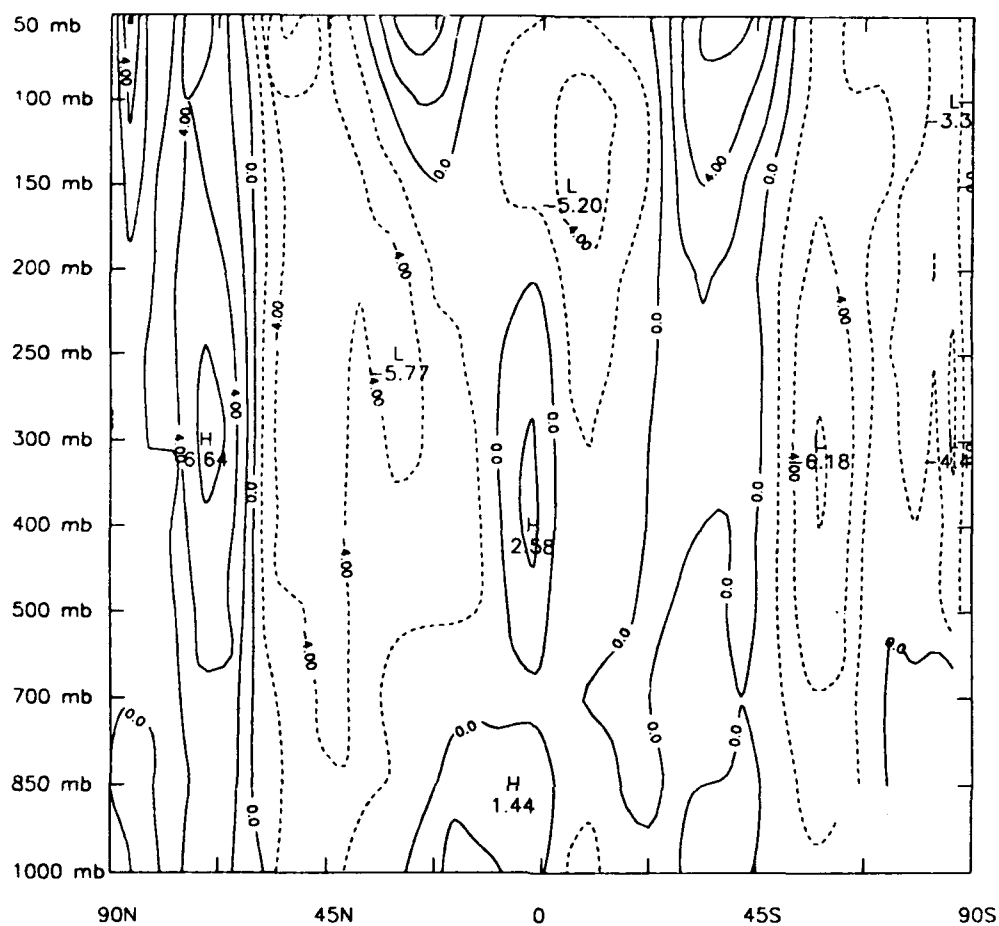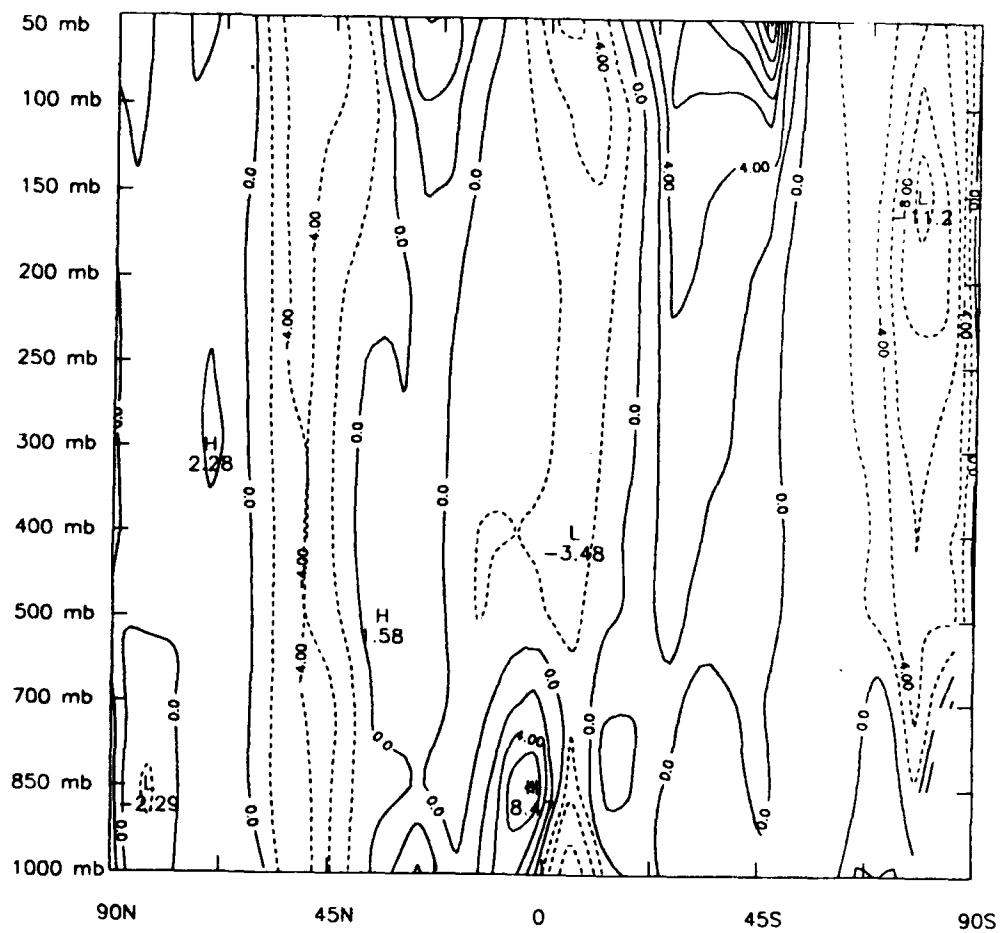
Figure 20b.   Same as Figure 19b except for t-values contour interval is 2.

hemisphere. The errors in the zonally averaged zonal wind are consistent with those of temperature errors to approximately satisfy the thermal wind relation. Extratropical systematic errors in day 10 forecast of 500 mb geopotential height and 850 mb temperatures in both the models are larger than those in tropics but they are not all significantly different from zero because the transient errors are also large. The tropical systematic errors in both the models appear significantly different from zero. One of the differences between the error characteristics of the two models is the magnitude of error in the tropics. The AFGL model tropical error magnitudes in 500 mb geopotential height, and 850 mb and 150 mb temperature are larger than the corresponding errors in the COLA model in some cases twice as large. There are large differences in the systematic error structure in 850 mb relative humidity between the two models. In the AFGL model negative errors are largely over ocean and positive errors are over land. In the COLA model the errors are largely positive with some small regions of negative errors. In the AFGL model the relative humidity errors appear rather serious. The model's tropical tropospheric temperature has a cold bias. Because the saturation vapor pressure decreases with temperature, one would expect positive error in the relative humidity as in the COLA model. The negative errors imply that lower troposphere over tropical oceans is very dry.

There are two major differences in the manner in which the physics is treated in these models. First is that the AFGL model does not include radiation interaction with deep convective clouds. Second is the manner in which the SST is prescribed. The $\sigma = 1$ surface in the model is determined by the prescribed orography in the spectral form. Due to the Gibbs oscillations there are some non-zero height values over the ocean. The SST prescribed form observations create fictitious horizontal temperature gradients on $\sigma = 1$ surface because it is lower or higher than the sea level. This can have an adverse effect on heat and moisture fluxes between the surface and the atmosphere. To minimize this effect the SST in the COLA model is interpolated to $\sigma = 1$ surface assuming uniform $6.5° K/km$

43

lapse rate. This modification in SST is not included in the AFGL model, but its effect is to some extent minimized by the smoothed orography. The tropical temperature errors in the AFGL could be reduced by including the convective cloud–radiation interaction. Heating at the cloud base in the lower troposphere and cooling at the cloud top in the lower stratosphere will improve the temperature forecast in the tropics. Interpolating the prescribed SST to $\sigma = 1$ level may improve the error in relative humidity and temperature over oceans. The AFGL model includes a shallow convection scheme based on an empirical relation derived from the GATE data (Mahrt *et al* 1987). It is possible that this parameterization is not as effective as the atmosphere in transporting heat and moisture from the surface to the atmosphere. The lack of vertical transport of heat and moisture may be responsible for the large errors in 850 mb temperature and relative humidity.

APPENDIX   A

SILHOUETTE OROGRAPHY REPRESENTATION

Highest resolution global orography data available at the present is the 10-minute elevation data from U.S. Navy. The fine orographic structure in the Navy data cannot be explicitly represented in models of present horizontal resolution. As mentioned in the Introduction the mean orography computed as an arithmetic average of points over the model grid underestimates the blocking effects of high mountains. In order to achieve the proper large scale effects of mountains the so called silhouette orography is computed by taking an average of maximum peaks of mountain profiles in the east-west and north-south directions over a grid box, that is,

$$Z_{sil} = \frac{1}{2} \left[\frac{1}{N} \sum_{j=1}^{N} ZI_j + \frac{1}{M} \sum_{i=1}^{M} ZJ_i \right] \tag{A-1}$$

where N and M are the number of subgrid profiles of mountain within a grid box in x and y directions, respectively. ZI is maximum height of the profile in the y-z plane, and similarly, ZJ is the maximum height of the profile in the x-z plane.

The silhouette orography computed from equation (A-1) is then represented in terms of the spherical harmonics. The number of harmonics used in the representation depends on the horizontal resolution of the model. Rhomboidal truncation at wave number 30 is used in the AFGL model. The truncation produces Gibbs oscillations in the representation. The amplitudes of the oscillations over ocean could be as large as 1 km. To reduce the amplitude of these oscillations a scale selective smoother, suggested by Hoskins (1980), is applied to the spectral

coefficients. The smoother is,

$$\exp(-k(n(n+1))^2)$$

where k is selected such that the highest retained coefficient is reduced to 0.1 of its initial value, and n is the degree of associated Legendre function. The smoothing function reduces the amplitude of oscillations over ocean and yields smoother topography field over continents without significantly reducing the enhanced effect of silhouette orography.

APPENDIX   B

PARAMETERIZATION OF OROGRAPHIC GRAVITY WAVE DRAG

As mentioned earlier, depending on atmospheric stability and vertical wind shear, gravity waves can propagate vertically to great heights until they are absorbed and/or reflected by critical layers, or they become unstable as a consequence of convective or shear instabilities, in which case the gravity waves dissipate. These waves transport momentum vertically and deposit it where they are dissipated. The level where they are dissipated the momentum is lost by the large-scale flow and it is brought down to the earth's surface where it is deposited. The parameterization of these effects in GCMs and NWP models are based on simplified theoretical concepts and observational evidence. The parameterization consists of determining the drag due to gravity waves at the surface and its vertical variation in the atmosphere. There are two approaches to parameterize the wave drag at the surface. One is based on linear theory (Palmer *et al.*,1986; McFarlane,1987) and the other is based on nonlinear theory (Pierrehumbert,1987). The vertical variation of the wave drag in the atmosphere depends on critical layers and convective or shear instabilities (Palmer *et al.*, 1986; Helfand *et al.*,1987). Here we present the parameterizations of the surface drag based both on the linear and nonlinear theories.

1. GRAVITY WAVE DRAG AT THE EARTH'S SURFACE

a)   Linear Theory

Let us consider a two dimensional, adiabatic, inviscid flow over a small mountain, 50 to 100 km wide. The governing equations for the mountain wave can be

written as:

$$\rho \frac{du}{dt} = - \frac{\partial p}{\partial x} \qquad \text{(B-1)}$$

$$\rho \frac{dw}{dt} = - \frac{\partial p}{\partial z} - \rho g \qquad \text{(B-2)}$$

$$\frac{d\rho}{dt} = - \rho (\frac{\partial u}{\partial x} + \frac{\partial w}{\partial z}) \qquad \text{(B-3)}$$

$$\frac{dp}{dt} = c^2 \frac{d\rho}{dt} \quad , \quad c^2 = \gamma RT \qquad \text{(B-4)}$$

$$p = \rho RT \qquad \text{(B-5)}$$

We shall express each variable as a sum of a basic state and a perturbation, where the basic state is given by,

$$\overline{U}(z), \quad \overline{T}(z)$$

$$\overline{W}(z) = 0$$

$$\frac{d\overline{p}}{dz} = - \overline{\rho} g$$

$$\overline{p} = \overline{\rho} R \overline{T}$$

Linearizing equations B-1 to B-5 and assuming a steady state condition, we have,

$$\overline{\rho} (\overline{U} \frac{\partial u'}{\partial x} + w' \frac{d\overline{U}}{dz}) = - \frac{\partial p'}{\partial x} \qquad \text{(B-6)}$$

$$\overline{\rho} \overline{U} \frac{\partial w'}{\partial x} = - \frac{\partial p'}{\partial z} - \rho' g \qquad \text{(B-7)}$$

48

$$\overline{U}\frac{\partial\rho'}{\partial x} + w'\frac{d\overline{\rho}}{dz} = -\overline{\rho}\left(\frac{\partial u'}{\partial x} + \frac{\partial w'}{\partial z}\right) \tag{B-8}$$

$$\overline{U}\frac{\partial p'}{\partial x} + w'\frac{d\overline{p}}{dz} = \overline{c}^2\left(\overline{U}\frac{\partial\rho'}{\partial x} + w'\frac{d\overline{\rho}}{dz}\right) \tag{B-9}$$

Equation (B-9) may be rewritten as,

$$\frac{\overline{U}}{\overline{\rho}}\frac{\partial\rho'}{\partial x} = w'\left(-\frac{1}{\overline{\rho}}\frac{d\overline{\rho}}{dz} - \frac{g}{\overline{c}^2}\right) + \frac{\overline{U}}{\overline{c}^2\overline{\rho}}\frac{\partial p'}{\partial x} \tag{B-10}$$

where the last term can be neglected, which implies that the pressure variations are not important in generation of density anomalies for low frequency motion. Define

$$\beta \equiv -\frac{1}{\overline{\rho}}\frac{d\overline{\rho}}{dz} - \frac{g}{\overline{c}^2} = \frac{1}{\overline{\theta}}\frac{d\overline{\theta}}{dz} \tag{B-11}$$

which is a measure of the static stability. The equations B-6 to B-10 can be reduced to obtain a single equation for vertical velocity $w'(x,z)$,

$$w'_{xx} + w'_{zz} - \overline{S}w'_z + \left(\frac{\beta g}{\overline{U}^2} + \frac{\overline{S}\,\overline{U}_z}{\overline{U}} - \frac{\overline{U}_{zz}}{\overline{U}}\right)w' \tag{B-12}$$
$$+ \frac{gw'}{\overline{c}^2}\left(\frac{1}{\overline{U}}\frac{d\overline{U}}{dz} + \frac{1}{w'}\frac{dw'}{dz} - S\right) = 0$$

where

$$\overline{S} = -\frac{d}{dz}\ln\overline{\rho}. \tag{B-13}$$

Let

$$\hat{w} \equiv \left[\overline{\rho}/\overline{\rho}_\bullet\right]^{\frac{1}{2}}w' \tag{B-14}$$

and neglect the last term of B-12, since $\dfrac{gw'}{\overline{c}^2} \sim \dfrac{10^2}{300^2} << 1$. Equation B-12 then becomes

$$\hat{w}_{xx} + \hat{w}_{zz} + l^2(z)\hat{w} = 0 \qquad \text{(B-15)}$$

where Scorer parameter is defined as,

$$l^2(z) \equiv \frac{\beta g}{\overline{U}^2} + \frac{\overline{S}\,\overline{U}_z}{\overline{U}} - \frac{1}{4}\overline{S}^2 + \frac{1}{2}\overline{S}_z - \frac{\overline{U}_{zz}}{\overline{U}}$$

Equation B-15 is well known as the linearized steady state equation for the vertical motion of gravity waves. In practice, $l^2(z)$ is usually dominated by the first term, *i.e.*, the buoyancy force term. Only in regions of strong shear will the term $\overline{U}_{zz}/\overline{U}$ become important. Neglecting the $\overline{S}$ terms is equivalent to making the Boussinesq approximation, that is, density variations are only important as they affect the buoyancy. To determine the lower boundary condition, the flow is assumed to follow the terrain at the ground, which is described by sinusoidal topography, $h_*(x) = h_m \sin kx$. The streamline slope equals the terrain slope:

$$\frac{w}{u} = \frac{w'}{\overline{U} + u'} = \frac{dh_*}{dx} \qquad (\text{ at } z = h_*(x)) \qquad \text{(B-16)}$$

$$= h_m k \cos kx. \qquad \text{(B-17)}$$

Assuming the amplitude of topography is small (as is disturbance u'), the lower boundary condition may be expressed as:

$$w' = \hat{w} = \overline{U} h_m k \cos kx \qquad \text{(B-18)}$$

In order to solve the equation B-15, we shall separate the variables, that is, let

$$\hat{w}(x,z) = \Phi_1(z) \cos kx + \Phi_2(z) \sin kx. \qquad \text{(B-19)}$$

Substituting B-19 into B-15 we get,

$$\Phi_{zz} + (l^2(z) - k^2)\Phi = 0. \qquad \text{(B-20)}$$

Both Φ_1 and Φ_2 satisfy equation (B-20). To satisfy the lower boundary condition, k should be the same as the terrain wave number. The sign of the term in

parentheses of the equation is important because it determines whether the stationary gravity waves are internal or external. Here we consider only vertically propagating internal gravity waves, *i.e.*, $k^2 < l^2$. If l is treated as piecewise constant as Scorer did, the solution of (B-20) is obtained as follows:

$$\Phi(z) = A \sin (l^2 - k^2)^{\frac{1}{2}} z + B \cos (l^2 - k^2)^{\frac{1}{2}} z$$

combining this with (B-19) gives

$$\hat{w}(x,z) = C \cos [kx + (l^2 - k^2)^{\frac{1}{2}} z] + D \cos [kx - (l^2 - k^2)^{\frac{1}{2}} z]$$
$$+ E \sin [kx + (l^2 - k^2)^{\frac{1}{2}} z] + F \sin [kx - (l^2 - k^2)^{\frac{1}{2}} z] \qquad \text{(B-21)}$$

Applying the lower boundary condition implies

$$E + F = 0$$
$$C + D = h_m k \overline{U}$$

The so-called radiation condition is imposed, *i.e.*, that there be no components of the flow which radiate energy downward.

$$D = F = 0$$

This last condition implies that

$$E = 0$$

and

$$C = h_m k \overline{U}.$$

Thus, equation (B-21) becomes

$$\hat{w}(x,z) = \overline{U} h_m k \cos [kx + (l^2 - k^2)^{\frac{1}{2}} z]. \qquad \text{(B-22)}$$

If the hydrostatic assumption is employed, it can be shown that $\hat{w}_{xx}$ is eliminated in

(B-15), such that k^2 disappears in (B-20) leading to the solution:

$$\hat{w}(x,z) = \overline{U} h_m k \cos(kx + lz)$$ (B-23)

where,

$$w'(x,z) = \left[\frac{\overline{\rho_*}}{\overline{\rho}}\right]^{\frac{1}{2}} \hat{w}(x,z) = \left[\frac{\overline{\rho_*}}{\overline{\rho}}\right]^{\frac{1}{2}} \overline{U} h_m k \cos(kx + lz)$$

Under the Boussinesq approximation, the continuity equation becomes

$$\frac{\partial u'}{\partial x} + \frac{\partial w'}{\partial z} = 0.$$ (B-24)

So there exists stream function which can be defined by

$$w' = \overline{U}\frac{\partial \psi}{\partial x}$$

$$u' = -\frac{\partial \overline{U}\psi}{\partial z}.$$

Thus

$$\psi = \int \frac{w'}{\overline{U}} dx = h \sin(kx + lz)$$ (B-25)

where, $h \equiv \left[\frac{\overline{\rho_*}}{\overline{\rho}}\right]^{\frac{1}{2}} h_m$, is the displacement amplitude of stream function.

$$u' = -\frac{\partial \overline{U}\psi}{\partial z}$$

$$= -\overline{U} h_z \sin(kx + lz) - \overline{U}_z h \sin(kx + lz)$$

$$-\overline{U} h l \cos(kx + lz)$$ (B-26)

The upward flux of momentum averaged over one horizontal wave length L now can be written as

$$\bar{\rho}\,\widehat{u'w'} = \frac{\bar{\rho}}{L}\int_0^L u'w'dx$$

$$= -\frac{\bar{\rho}}{L}(h\,\bar{U}k\,(\bar{U}_z h + \bar{U}h_z))\int_0^L \sin(kx+lz)\cos(kx+lz)\,dx$$

$$-\frac{\bar{\rho}}{L}\bar{U}^2 h^2 k\,l\int_0^L \cos(kx+lz)^2\,dx$$

Since $\int_0^L \sin(kx+lz)\cos(kx+lz)\,dx = 0$,

$$\bar{\rho}\,\widehat{u'w'} = -\frac{\bar{\rho}}{L}\bar{U}^2 h^2 kl\int_0^L \frac{1}{2}(1-\cos(2(kx+lz)))\,dx$$

$$= -\frac{\bar{\rho}}{2}\bar{U}^2 h^2 kl \tag{B-27}$$

Recall,

$$l^2 \approx \frac{\beta g}{\bar{U}^2} = \frac{N^2}{\bar{U}^2}$$

where N is the Brunt – Väisälä frequency. Substituting this into (B-27) we obtain the gravity wave drag at the surface as follow:

$$\tau = -\bar{\rho}\,\widehat{u'w'}$$

$$= \frac{\bar{\rho}}{2}k\,h^2\bar{U}\,N$$

$$= \kappa\bar{\rho}\,h^2\bar{U}\,N \tag{B-28}$$

where $\kappa = \frac{1}{2}k$. The horizontal characteristic subgrid-scale wavelength is

$$L = \frac{2\pi}{k} = 125\text{ km}$$

so that

$$\kappa = 2.5\times 10^{-5}\text{ m}^{-1}$$

h^2, the variance of subgrid-scale orography, is computed from 10-minute elevation data from the U. S. Navy. $\overline{U}$, $\overline{\rho}$ and N are the model variables. In order to avoid numerical instabilities, h is limited to a maximum value of 400 m. In addition, the linear theory requires that Froude number,

$$Fr = \frac{Nh}{\overline{U}} < 0.8$$

If Fr exceeds 0.8 nonlinear effects become important. Therefore, wherever Fr exceeds 0.8 the surface drag, which depends on h^2, is reduced by a factor $(0.8/Fr)^2$. That is,

$$Max\,(h) = min\,\{0.8\,\frac{\overline{U}}{N},\,400\,m\}.$$

b) Nonlinear Theory

The parameterization of surface wave drag,

$$\tau = \kappa\overline{\rho}N\overline{U}h^2 \qquad\qquad (B\text{-}29)$$

based on the linear theory, is valid only for

$$Fr = \frac{Nh}{\overline{U}} < 0.8.$$

Pierrehumbert(1987) has argued that very close to the surface where $\overline{U}$ is small and in the vicinity of mountains with large h Fr exceeds 0.8 and hence the linear theory is not valid. He proposed a parameterization of surface wave drag to include situations where Fr is greater than 0.8. It is based on dimensional considerations and results from numerical experiments.

$$|\tau| = \overline{\rho u'w'} = \frac{1}{\Delta x}\int \rho u'w'dx \qquad\qquad (B\text{-}30)$$

where, Δx is grid length of the model. Equation (B-30) can be written as

$$|\tau| \propto \frac{1}{\Delta x} \bar{\rho}[u'][w']L \tag{B-31}$$

where, L is the length scale of mountain. Let,

$$[u'] = \bar{U} \tag{B-32}$$

$$h = \frac{\bar{U}}{N} \tag{B-33}$$

$$[w'] = \frac{h}{L}[u'] = \frac{h}{L}\bar{U} = \frac{\bar{U}^2}{LN} \tag{B-34}$$

Substituting (B-32) and (B-34) in (B-31), we get

$$|\tau| \propto \left[\frac{\bar{\rho}\bar{U}^3}{\Delta x\, N}\right] \tag{B-35}$$

or

$$|\tau| = \frac{\bar{\rho}\bar{U}^3}{\Delta x\, N} G(Fr) \tag{B-36}$$

where, G(Fr) is a monotonically increasing function of Fr. The functional form of G(Fr), determined from numerical experiments, is

$$G(Fr) = \left[\frac{Fr^2}{1 + Fr^2}\right].$$

If there are m mountains in a grid box,

$$|\tau| = \frac{m}{\Delta x}\left[\bar{\rho}\frac{\bar{U}^3}{N}\right]\left[\frac{Fr^2}{1 + Fr^2}\right] \tag{B-37}$$

$$= \left[\frac{\bar{\rho}\bar{U}^3}{L}N\right]\left[\frac{Fr^2}{1 + Fr^2}\right] \tag{B-38}$$

where, L corresponds to wavelength of monochromatic wave in the direction of the surface wind. The equation (B-38) is valid for a wide range of values of Fr. For values of Fr less than 0.8 where linear theory is valid, the equation (B-38) reduces to

$$|\tau| = \bar{\rho}\kappa\bar{U}Nh^2$$

which is the same as (B-28) the parameterization based on linear theory.

Pierrehumbert(1987) has shown that the nonlinear effects can lead to large changes in the character of the flow and amplification of wave drag close to the surface. To account for the nonlinear amplification a base layer is defined to compute the surface wave drag. The base layer is approximately the first third of the atmosphere. We have taken this layer to be from surface to 642 mb. The surface drag is computed from equation B-38 by using mass weighted model variables over the the depth of the base layer. L is equal to 125 km as before. Also, in this case the maximum value of h is restricted to 400 m for numerical stability.

2. GRAVITY WAVE DRAG IN THE ATMOSPHERE

Eliassen and Palm(1961) have shown that in absence of transience and turbulent dissipation the momentum flux is independent of height. In such a case the momentum flux is deposited in the top layer of the model and hence there is no body force in the model atmosphere because the vertical variation of momentum flux, $\frac{\partial\tau}{\partial\sigma}$, vanishes. The momentum flux can vary in vertical if one or more of the following conditions occur: (i) wave-modified Richardson number, Ri_m, is less then the critical Richardson number, Ri_c, (ii) shear instabilities ($Ri < 1/4$) create turbulence, (iii) convective instabilities ($Ri < 0$) create turbulence and (iv) critical level where direction of the wind is perpendicular to surface wind or greater than 90 degrees.

The wave-modified Richardson number can be expressed in terms of the Richardson number for the undisturbed state of the atmosphere. The

56

Brunt – Väisälä frequency is

$$N_T{}^2 \equiv \frac{g}{\theta_T} \frac{d\theta_T}{dz} \tag{B-39}$$

where the subscript T refers to the sum of the background flow and wave contribution, *i. e.*

$$\theta_T = \bar{\theta} + \theta'$$

$$N_T{}^2 = \frac{g}{\bar{\theta} + \theta'} \left(\frac{d\bar{\theta}}{dz} + \frac{d\theta'}{dz} \right). \tag{B-40}$$

Under the adiabatic approximation the thermodynamic equation can be written as

$$\bar{U} \frac{\partial \theta'}{\partial x} + w' \frac{\partial \bar{\theta}}{\partial z} = 0 \tag{B-41}$$

So θ' can be written in terms of stream function,

$$\theta' = - \psi \frac{d\bar{\theta}}{dz} \tag{B-42}$$

thus

$$N_T{}^2 = \frac{g}{\bar{\theta} + \theta'} \left[\left(1 - \frac{d\psi}{dz} \right) \frac{d\bar{\theta}}{dz} - \psi \frac{d^2\bar{\theta}}{dz^2} \right] \tag{B-43}$$

Neglecting the second order derivative term and approximating

$$\frac{1}{\bar{\theta} + \theta'} \simeq \frac{1}{\bar{\theta}}$$

we get,

$$N_T{}^2 = \frac{g}{\bar{\theta}} \left[1 - \frac{d\psi}{dz} \right] \frac{d\bar{\theta}}{dz} \tag{B-44}$$

Referring back to equation B-25 that

$$\psi = h \sin (kx + lz) \tag{B-45}$$

thus

$$N_T^2 = N^2 (1 - h\,l\cos(kx + lz) + h_z \sin(kx + lz))$$

$$= N^2 (1 - \frac{Nh}{\overline{U}}\cos(kx + lz) - \frac{1}{2}\frac{hN}{g}\sin(kx + lz))$$

$$> N^2 (1 - \frac{Nh}{\overline{U}}) \equiv N_m^2 \qquad (B\text{-}46)$$

where $N = \frac{g}{\overline{\theta}}\frac{d\overline{\theta}}{dz}$ which is calculated from the mean flow. The term $-N^2(\frac{Nh}{\overline{U}})$

can be regarded as the influence at the phase of the (monochromatic) wave for which the decrease in the local static stability is maximized. Finally, the wave modified Richardson number is

$$R_{im} \equiv \frac{N_m^2}{(\frac{\partial \overline{U}}{\partial z})^2} = R_i (1 - \frac{Nh}{\overline{U}}) \qquad (B\text{-}47)$$

This implies that for small values of $\overline{U}$ wave breaking will occur even for mountains of relatively moderate heights. The critical Froude number, Fr_c, for breaking can be written as

$$Fr_c = Nh_c/\overline{U} = 1 - Ri_c / Ri = 1 - 1/4\,Ri \qquad (B\text{-}48)$$

Once the gravity wave begins to break, the wave saturation hypothesis of Lindzen (1981) is invoked, in which it is assumed that the wave-induced turbulent dissipation prevents the displacement amplitude, h, from exceeding its critical value h_c, that is,

$$h_c = Fr_c\overline{U} / N = (Fr_c\overline{U} / Nh) = (Fr_c / Fr)h$$

Replacing h by h_c in equation (B-28) we have

$$\tau_c = \rho\overline{U}N\kappa h_c^2 = \rho\overline{U}N\kappa h^2(Fr_c / Fr)^2 = \tau (Fr_c / Fr)^2 \qquad (B\text{-}49)$$

This implies that if the computed value of Fr at a given level exceeds critical value,

58

Fr_c,

it is assumed that the turbulence generated by the breaking wave will reduce the wave momentum flux by the factor $(Fr_c/Fr)^2$. However, h the displacement of isentropic surface on a particular level is not known. The following procedure is used to calculate Fr. From equation (B-28), we have

$$\tau = \kappa \rho \overline{U} N h^2$$
$$h^2 = \frac{\tau}{\kappa \rho \overline{U} N} = \frac{h \tau}{\kappa \rho \overline{U}^2 Fr}$$
$$h = \frac{\tau}{\kappa \rho \overline{U}^2 Fr}$$

Substitute this relation of h into the definition of Froude number $Fr = hN/\overline{U}$ we obtain the expression for the square of the Froude number,

$$Fr^2 = \frac{\tau N}{\kappa \rho \overline{U}^3} \qquad\qquad (B\text{-}50)$$

Very close to the surface convective and shear instabilities occur frequently and dissipate the momentum. In order to allow gravity waves to propagate vertically through boundary layer the parameterization based on nonlinear theory where the base layer extends from surface to 642 mb the momentum flux in the base layer can change only due to wave saturation, that is, if $Ri_m < Ri_c$. Here the effects of shear and convective instabilities or critical levels are ignored.

After the vertical profile of the momentum flux has been determined, the influence of the gravity wave drag on the large scale flow is determined by the vertical wave momentum flux divergence.

59

APPENDIX C

COMPUTER CODE FOR OROGRAPHIC GRAVITY

WAVE DRAG PARAMETERIZATION

```
      SUBROUTINE GWDD(PSFC,U,V,TT,CHUG,CHVG,IMX,KMAX,LATCO)
      DIMENSION XTENS(96,19),YTENS(96,19)
      DIMENSION RO(96,18),PP(96,18),TENSIO(96,19)
      DIMENSION SLEV(19),SLAY(18)
      DIMENSION DZ(96,18),PPP(96,19)
      DIMENSION DRAGSF(96),XDRAG(96),YDRAG(96)
      DIMENSION TT(IMX,KMAX),T(98,18),
     1       U(IMX,KMAX),V(IMX,KMAX),PSFC(IMX)
      DIMENSION CHUG(IMX,KMAX),CHVG(IMX,KMAX)
      COMMON /SF/ VAR(96,80),DOIT,UTEN(96,80,18),
     1       VTEN(96,80,18),TAUSX(96,80),TAUSY(96,80)
      INTEGER DOIT
      REAL LSTAR,NBAR,BV(18)


C ***************************************************************
C
C                   INPUT PARAMETERS
C
C    PSFC    SURFACE PRESSURE
C    U       ZONAL WIND
C    V       MERIDIONAL WIND
C    TT      VIRTUAL TEMPERATURE
C    IMX     NUMBER OF GRID POINTS ALONG LONGITUDE
C    KMAX    LEVELS IN THE VERTICAL
C    LATCO   NUMBER OF GAUSSIAN COLATITUDES
C    VAR     OROGRAPHICAL VARIANCE
C
C
C                   OUTPUT PARAMETERS
C
C    UTEN    U TENDENCY
C    VTEN    V TENDENCY
C
C ***************************************************************
```

```
        MLONG= 96
        DO 123 I= MLONG+ 1,IMX
        DO 123 K= 1,KMAX
          CHUG(I,K)= 0.0
          CHVG(I,K)= 0.0
123     CONTINUE


        DO 124 I= 1,MLONG
        DO 124 K= 1,KMAX
          T(I,K)= TT(I,K)
124     CONTINUE


        DO 2000 I= 1,MLONG
          PSFC(I)= EXP(PSFC(I))*10.0
2000    CONTINUE


        MLAT= 80
        NLAY= 18
        NLAYM1= NLAY-1
        NLAYP1= NLAY+ 1
        DLON= 360.0/96.0
        DLAT= 180.0/80.0
        GRAV= 9.81
        AGRAV= 1.0/GRAV
        RGAS= 287.0
        PTOP= 10.0
        ICOUNT= 0


        SLEV(19)= 0.0
        SLEV(18)= 0.05
        SLEV(17)= 0.1
        SLEV(16)= 0.15
        SLEV(15)= 0.2
        SLEV(14)= 0.25
        SLEV(13)= 0.3
        SLEV(12)= 0.35
        SLEV(11)= 0.4
        SLEV(10)= 0.45
        SLEV(9)= 0.546
        SLEV(8)= 0.642
        SLEV(7)= 0.735
        SLEV(6)= 0.82
```

```
      SLEV(5)= 0.893
      SLEV(4)= 0.948
      SLEV(3)= 0.973
      SLEV(2)= 0.99
      SLEV(1)= 1.0

      SLAY(18)= 0.021
      SLAY(17)= 0.074
      SLAY(16)= 0.124
      SLAY(15)= 0.175
      SLAY(14)= 0.225
      SLAY(13)= 0.275
      SLAY(12)= 0.325
      SLAY(11)= 0.375
      SLAY(10)= 0.425
      SLAY(9)= 0.497
      SLAY(8)= 0.594
      SLAY(7)= 0.688
      SLAY(6)= 0.777
      SLAY(5)= 0.856
      SLAY(4)= 0.920
      SLAY(3)= 0.960
      SLAY(2)= 0.981
      SLAY(1)= 0.995

C     INTERNAL CONSTANTS

      INSTAB= 0
      ICRILV= 0
      NLEV= NLAY
      NLEVM1= NLAYM1
      NLEVP1= NLAYP1
      AKWNMB= 2.5E-05
      LSTAR= 1.0/AKWNMB
      GOCP= GRAV/1005.
      NBASE= 8
      NBASEP1= NBASE+ 1
      NBASEM1= NBASE-1

C     CONSTRAIN THE VARIENCE

      III= MLAT+ 1-LATCO
         DO 4 J= 1,MLONG
               IF(VAR(J,III).GT.160000.)VAR(J,III)= 160000.0
```

```
4        CONTINUE

C       COMPUTE PRESSURE AT EVERY LAYER

        DO 7 LAY= 1,NLAY
            DO 9 J= 1,MLONG
                PP(J,LAY)= SLAY(LAY)*PSFC(J)
9           CONTINUE
7       CONTINUE

C       COMPUTE PRESSURE AT EVER LEVEL

        DO 70 LEV= 1,19
        DO 70 J= 1,MLONG
            PPP(J,LEV)= SLEV(LEV)*PSFC(J)
70      CONTINUE

C       COMPUTE DENSITY AT EVERY LAYER

        DO 10 LAY= 1,NLAY
            DO 12 J= 1,MLONG
                PRCB= PP(J,LAY)
                RT= RGAS*T(J,LAY)
                RO(J,LAY)= PRCB/RT
12          CONTINUE
10      CONTINUE

C       COMPUTE DZ AT EVERY LEVEL FROM 2 TO 18

        DO 14 J= 1,MLONG
            ROILO= 1.0/RO(J,1)
            DO 15 LL= 2,NLEV
                ROIUP= 1.0/RO(J,LL)
                ROIAVE= (ROILO+ ROIUP)*0.5
                X= PP(J,LL-1)-PP(J,LL)
                DZ(J,LL)= AGRAV*ROIAVE*X
                ROILO= ROIUP
15          CONTINUE
14      CONTINUE

C       END OF INPUT AND ELEMENTARY COMPUTATIONS

        III= MLAT+ 1-LATCO
```

```fortran
      DO 17 J= 1,MLONG

C*******************************************************
C     SURFACE AND BASE LAYER STRESS              *
C*******************************************************

C     BASE LAYER STRESS IS DEFINED IN TERMS OF A VERTICAL AVE.

      ROBAR= 0.0
      UBAR= 0.0
      VBAR= 0.0
      DO 200 L= 1,NBASEM1

C        MASS WEIGHTED VERITCAL AVERAGE OF DENSITY, VELOCITY

      ROBAR= ROBAR+ RO(J,L)*(PPP(J,L)-PPP(J,L+ 1))
      UBAR= UBAR+ U(J,L)*(PPP(J,L)-PPP(J,L+ 1))
      VBAR= VBAR+ V(J,L)*(PPP(J,L)-PPP(J,L+ 1))

200      CONTINUE
      ROBAR= ROBAR/(PPP(J,1)-PPP(J,NBASE))
      ROBAR= ROBAR*100.0
      UBAR= UBAR/(PPP(J,1)-PPP(J,NBASE))
      VBAR= VBAR/(PPP(J,1)-PPP(J,NBASE))

C    END VERTICAL AVERAGE

C        VAISALA FREQUENCY

      DO 201 LEV= 2,NBASE
        LAY= LEV
        VAI1= (T(J,LAY)-T(J,LAY-1))
1        /DZ(J,LEV)+ GOCP

        IF(VAI1.LT.0.0)THEN
          VAI1= 0.0
        ENDIF

        VAI2= 2.0*GRAV/(T(J,LAY)
1          + T(J,LAY-1))
        VSQUA= VAI1*VAI2
        BV(LEV)= SQRT(VSQUA)
201      CONTINUE
```

```
C       VERTICAL MASS WEIGHTED AVERAGE OF THE BRUNT-VAISIALA
C       FREQ.

        NBAR= 0.0
        DO 202 LEV= 2,NBASE
          LAY= LEV
          NBAR= NBAR+ BV(LEV)*(PP(J,LAY-1)-PP(J,LAY))
202       CONTINUE
        NBAR= NBAR/(PP(J,1)-PP(J,NBASE))
        IF(NBAR.LE.0.0000001) THEN
          PRINT*,'NBAR IN GWD IS ZERO'
        ENDIF


C       DEFINITION OF SURFACE WIND VECTOR

        UUS= UBAR
        VVS= VBAR
        SPEEDS= SQRT(UUS*UUS+ VVS*VVS)
        IF(SPEEDS.EQ.0.0)THEN
          PRINT*,'SPEEDS EQ ZERO IN GWD'
        ENDIF
        ANG= ATAN2(VVS,UUS)
        ANGDEG= 180./3.1415926*ANG


C       STRESS AT THE SURFACE LEVEL LEV= 1

        FRSF= NBAR*SQRT(VAR(J,III))/SPEEDS
        IF(SPEEDS.EQ.0.0)THEN
        TENSIO(J,1)= 0.0
          ELSEIF(NBAR.NE.0.0)THEN
        GSTAR= GG(FRSF)
        TENSIO(J,1)= GSTAR*(ROBAR*SPEEDS*SPEEDS*SPEEDS)/
     1  (NBAR*LSTAR)
        ELSE
          TENSIO(J,1)= 0.0
        ENDIF

        XTENS(J,1)= COS(ANG)*TENSIO(J,1)
        YTENS(J,1)= SIN(ANG)*TENSIO(J,1)


C       SAVE SURFACE VALUES

        DRAGSF(J)= TENSIO(J,1)
        XDRAG(J)= XTENS(J,1)
```

```
        YDRAG(J)= YTENS(J,1)

        ROLO= RO(J,2)
        UULO= U(J,2)
        VVLO= V(J,2)
        TENSIO(J,2)= TENSIO(J,1)
        XTENS(J,2)= XTENS(J,1)
        YTENS(J,2)= YTENS(J,1)

C    SCALAR PRODUCT OF LOWER WIND VECTOR AND SURFACE WIND

        SCALLO= UULO*UUS+ VVLO*VVS

        DO 181 LEV= 3,NBASE
          LAY= LEV
          ROUP= RO(J,LAY)
          ROAVE= 0.5*(ROLO+ ROUP)

C    CONVERT TO NEWTON/M2

          ROAVE= 100.0*ROAVE

C    VELOCITY COMPONENT PARALELL TO SURFACE VELOCITY

          UUUP= U(J,LAY)
          VVUP= V(J,LAY)
          SCALUP= UUUP*UUS+ VVUP*VVS
          VELCO= 0.5*(SCALUP+ SCALLO)/SPEEDS

C    TAU DOESN'T CHANGE IN THE BASE LAYER BECAUSE OF A
C    CRITICAL LEVEL I.E. VELCO <  0.0

          IF(VELCO.LE.0.0)THEN
            TENSIO(J,LEV)= TENSIO(J,LEV-1)
            GOTO 1500
          ENDIF

C    FROUDE NUMBER SQUARED

      YY= BV(LEV)
      FRO2= YY/(AKWNMB*ROAVE*VELCO*VELCO*VELCO)
     1   *TENSIO(J,LEV-1)

C    DENOMINATOR OF RICHARDSON NUMBER
```

```
          DELUU= UUUP-UULO
          DELVV= VVUP-VVLO
          DELVE2= (DELUU*DELUU+ DELVV*DELVV)


C     RICHARDSON NUMBER

          IF(DELVE2.NE.0.0)THEN
             DELZ= DZ(J,LEV)
             VSQUA= BV(LEV)*BV(LEV)
             RICHSN= DELZ*DELZ*VSQUA/DELVE2
          ELSE
             RICHSN= 99999.0
          ENDIF


C     TAU IN THE BASE LAYER DOES NOT CHANGE BECAUSE OF THE
C     RICHARDSON CRITERION

          IF(RICHSN.LE.0.25)THEN
             TENSIO(J,LEV)= TENSIO(J,LEV-1)
             GO TO 1500
          ENDIF


C     TAU IN THE BASE LAYER DOES CHANGE IF THE LOCAL FROUDE
C     EXCEDES THE CRITICAL FROUDE NUMBER... THE SO CALLED
C     FROUDE NUMBER REDUCTION.

          CRIFRO= 1.0-0.25/RICHSN
          CRIF2= CRIFRO*CRIFRO
          IF(LEV.EQ.2)CRIF2= AMIN1(0.7,CRIF2)

          IF(FRO2.GT.CRIF2)THEN
             TENSIO(J,LEV)= CRIF2/FRO2*TENSIO(J,LEV-1)
             GO TO 1500
          ELSE
             TENSIO(J,LEV)= TENSIO(J,LEV-1)
             GOTO 1500
          ENDIF

1500         CONTINUE
          XTENS(J,LEV)= TENSIO(J,LEV)*COS(ANG)
          YTENS(J,LEV)= TENSIO(J,LEV)*SIN(ANG)
          ROLO= ROUP
          UULO= UUUP
```

```
                 VVLO= VVUP
                 SCALLO= SCALUP
181              CONTINUE


C**********************************************************************
C        STRESS FROM BASE LEVEL TO TOP LEVEL
C**********************************************************************

                 ICRILV= 0
                 INSTAB= 0
                 ROLO= RO(J,NBASE)
                 UULO= U(J,NBASE)
                 VVLO= V(J,NBASE)

C      SCALAR PRODUCT OF LOWER WIND VECTOR AND SURFACE WIND

                 SCALLO= UULO*UUS+ VVLO*VVS

                 DO 18 LEV= NBASEP1,NLAY+ 1
                   LAY= LEV

C      THE STRESS IS ALWAYS INITIALIZED TO ZERO

                 TENSIO(J,LEV)= 0.0
                 IF(ICRILV.EQ.1)THEN
                     GO TO 130
                 ENDIF
                 IF(LEV.NE.19)THEN
                     GO TO 150
                 ENDIF
                 TENSIO(J,LEV)= 0.0
                 GO TO 130
150               CONTINUE

                 ROUP= RO(J,LAY)
                 ROAVE= 0.5*(ROLO+ ROUP)

C      CONVERT TO NEWTON/M2

                 ROAVE= 100.0*ROAVE

C      VAISALA FREQUENCY

                 VAI1= (T(J,LAY)-T(J,LAY-1))
```

```
1              / DZ(J,LEV)+ GOCP

          IF( VAI1.LT.0.0)THEN
            ICRILV= 1
            TENSIO(J,LEV)= 0.0
            GO TO 130
          ENDIF

          VAI2= 2.0*GRAV/(T(J,LAY)
1           + T(J,LAY-1))
          VSQUA= VAI1*VAI2

C     VAISD IS THE BRUNT-VAISALA FREQUENCY N

          VAISD= SQRT(VSQUA)

C     VELOCITY COMPONENT PARALELL TO SURFACE VELOCITY

          UUUP= U(J,LAY)
          VVUP= V(J,LAY)

C     SCALAR PRODUCT OF UPPER AND SURFACE WIND VECTOR

          SCALUP= UUUP*UUS+ VVUP*VVS
          VELCO= 0.5*(SCALUP+ SCALLO)/SPEEDS
          IF( VELCO.LT.0.0)THEN
            ICRILV= 1
            TENSIO(J,LEV)= 0.0
            GO TO 130
          ENDIF

C     FROUDE NUMBER SQUARED

     YY= VAISD
     FRO2= YY/(AKWNMB*ROAVE*VELCO*VELCO*VELCO)
C  1    *TENSIO(J,LEV-1)

C     DENOMINATOR OF RICHARDSON NUMBER

          DELUU= UUUP-UULO
          DELVV= VVUP-VVLO
          DELVE2= (DELUU*DELUU+ DELVV*DELVV)

C     RICHARDSON NUMBER
```

69

```fortran
            IF(DELVE2.NE.0.0)THEN
               DELZ= DZ(J,LEV)
               RICHSN= DELZ*DELZ*VSQUA/DELVE2
            ELSE
               RICHSN= 99999.0
               ICOUNT= ICOUNT+ 1
            ENDIF
            IF(RICHSN.LE.0.25)THEN
               TENSIO(J,LEV)= 0.0
               ICRILV= 1
               GO TO 130
            ENDIF

C    CRITICAL FROUDE NUMBER

            CRIFRO= 1.0-0.25/RICHSN
            CRIF2= CRIFRO*CRIFRO

C    END CRITICAL FROUDE NUMBER

            IF(FRO2.GE.CRIF2)THEN
                GO TO 120
            ENDIF
            TENSIO(J,LEV)= TENSIO(J,LEV-1)
            GO TO 130
120         TENSIO(J,LEV)= CRIF2/FRO2*TENSIO(J,LEV-1)
130         CONTINUE
            XTENS(J,LEV)= TENSIO(J,LEV)*COS(ANG)
            YTENS(J,LEV)= TENSIO(J,LEV)*SIN(ANG)
            ROLO= ROUP
            UULO= UUUP
            VVLO= VVUP
            SCALLO= SCALUP
18          CONTINUE
17       CONTINUE

C        END STRESS

         DO 20 LAY= 3,NLAY
            DO 21 J= 1,MLONG
               LEV= LAY+ 1
               COEF= GRAV/PSFC(J)*.01
               DSIGMA= SLEV(LEV)-SLEV(LEV-1)
```

```fortran
      CHUG(J,LAY)= COEF/DSIGMA*(XTENS(J,LEV)-XTENS(J,LEV-1))
      CHVG(J,LAY)= COEF/DSIGMA*(YTENS(J,LEV)-YTENS(J,LEV-1))
21       CONTINUE
20      CONTINUE

      DSIGMA= SLEV(3)-SLEV(1)
      DO 444 J= 1,MLONG
        COEF= GRAV/PSFC(J)*.01
        CHUG(J,1)= COEF/DSIGMA*(XTENS(J,3)-XTENS(J,1))
        CHVG(J,1)= COEF/DSIGMA*(YTENS(J,3)-YTENS(J,1))
        CHUG(J,2)= CHUG(J,1)
        CHVG(J,2)= CHVG(J,1)
444    CONTINUE

      III= MLAT+ 1-LATCO

C   ZNORM= # OF DAYS * # OF STEPS PER DAY

      ZNORM= 10.0*96.0

      DO 333 J= 1,96
      DO 333 K= 1,18
        UTEN(J,III,K)= UTEN(J,III,K)+ CHUG(J,K)/ZNORM
        VTEN(J,III,K)= VTEN(J,III,K)+ CHVG(J,K)/ZNORM
333    CONTINUE

      DO 334 J= 1,96
        TAUSX(J,III)= TAUSX(J,III)+ XDRAG(J)/ZNORM
        TAUSY(J,III)= TAUSY(J,III)+ YDRAG(J)/ZNORM
334    CONTINUE

      RETURN
      END

      FUNCTION GG(FR)
      REAL FR
      G= 1.0
      A= 1.0
      GG= (FR*FR)/(FR*FR+ A*A)
      RETURN
      END
```

REFERENCES

Anthes, R. A., 1977: A cumulus parameterization scheme utilizing a one–dimensional cloud model. *Mon. Wea. Rev.*, **105**, 270–286.

Arpe, K. and E. Klinker, 1986: Systematic errors in the ECMWF operational model in mid–latitudes. *Quart. J. R. Met. Soc.*, **112**, 181–202.

Bettge, T. N., 1983: A systematic error comparison between the ECMWF and NMC prediction models. *Mon. Wea. Rev.*, **111**, 2385–2389.

Eliassen, A. and E. Palm, 1961: On the transfer of energy in stationary mountain waves. *Geofys. Pub.*, **22**, 1–23.

Epstein, E. S., 1988: How systematic are systematic errors? *Preprints of Eighth Conference on Numerical Weather Prediction*, February 22–26, 1988, Baltimore, MD.

Fawcett, E. B., 1969: Systematic errors in operational baroclinic prognoses at the National Meteorological Center. *Mon. Wea. Rev.*, **97**, 670–682.

Ferranti, L., T. N. Palmer, F. Molteni and E. Klinker, 1990: Tropical, extratropical interaction associated with the 30–60 day oscillation, and its impact on medium and extended range predictability. *J. Atmos. Sci.*, **47**, 2177–2199.

Geleyn, J. F., 1981: Some diagnostics of the cloud radiation interaction on ECMWF forecasting model. *ECMWF Workshop on radiation and cloud–radiation–interaction in numerical modeling*, pp. 135–162.

Harr, P. A., T. L. Tsui and L. R. Brody, 1983: Identification of systematic errors in a numerical weather forecast, *Mon. Wea. Rev.*, **111**, 1219–1227.

Harshvardhan, R. Davis, D. A. Randall and T. G. Corsetti, 1987: A fast radiation parameterization for general circulation models. *J. Geoph. Res.*, **92**, 1009–1016.

Heckley, W. A., 1985: Systematic errors of ECMWF operational forecasting model in tropical regions. *Q. J. R. Meteorol. Soc.*, **111**, 709–738.

Helfand, H. M., J. C. Jusem, S. Pfaendtner, J. Tenenbaum and E. Kalnay, 1987: The effect of a gravity wave drag parameterization on GLA fourth order GCM forecasts. *Short and Medium–Range Numerical Weather Prediction Collection of Paper Presented at the WMO/IUGG NWP Symposium*, Tokyo, 4–8 August 1986.

Hollingsworth, A., K. Arpe, M. Tiedtke, M. Capaldo and H. Savijärvi, 1980: The performance of a medium–range forecast model in winter – Impact of physical parameterization. *Mon. Wea. Rev.*, **108**, 1736–1773.

Hoskins, B. J., 1980: Representation of the earth topography using spherical harmonics. *Mon. Wea. Rev.*, **108**, 111–115.

Hou, Y.-T., 1990: Cloud–Radiation–Dynamics Interaction. Ph.D. Dissertation, Department of Meteorology, University of Maryland, College Park, MD.

Iwasaki, T., S. Yamada and K. Tada, 1989: A parameterization scheme of orographic gravity wave drag with two different vertical partitionings. Part I: Impact on medium–range forecasts. *J. Meteor. Soc. Japan*, **67**, 11–27.

Kirtman, B., A. Vernekar, D. DeWitt and J. Zhou, 1991: Impact of orographic gravity wave drag on extended–range forecasts with the COLA–GCM. (Submitted to *Mon. Wea. Rev.* for publication)

Krishnamurti, T. N., M. Kanamitsu, R. Godbole, C.-B. Chang, F. Carr and J. H. Chow, 1976: Study of monsoon depression (II), Dynamical Structure. *J. Meteor. Soc. Japan*, **54**, 208–225.

Kuo, H. L., 1965: On formation and intensification of tropical cyclones through latent heat release by cumulus convection. *J. Atmos. Sci.*, **22**, 40–63.

Kuo, H. L., 1974: Further studies of the parameterization of the influence of cumulus convection on large–scale flow. *J. Atmos. Sci.*, **31**, 1232–1240.

Lacis, A. and J. E. Hansen, 1974: A parameterization of absorption of solar radiation in the earth's atmosphere. *J. Atmos. Sci.*, **31**, 118–133.

Lambert, S. J. and P. E. Merilees, 1978: A study of planetary wave errors in a spectral numerical weather prediction model. *Atmosphere–Ocean*, 16, 197–211.

Leith, C. E., 1971: Atmospheric predictability and two–dimensional turbulence. *J. Atmos. Sci.*, 28, 145–161.

Lilly, D. K., 1972: Wave momentum flux: A GARP problem. *Bull. Amer. Meteor.c.*, 20, 17.

Lindzen, R. S., 1981: Turbulence and stress due to gravity wave tidal breakdown. *J. Geophys. Res.*, 86, 9707–9714.

Liou, K.–N. and S. C. Ou, 1981: Parameterization of infrared radiative transfer in cloudy atmospheres. *J. Atmos. Sci.*, 38, 2707–2716.

Livezy, R. and W. Y. Chen, 1983: Statistical field significance and its determination by Monte Carlo techniques. *Mon. Wea. Rev.*, 111, 46–59.

Lorenz, E. N., 1969: The predictability of a flow which possesses many scales of motion. *Tellus*, 21, 289–307.

Louis, J.–F., 1979: A parametric model of vertical eddy fluxes in the atmosphere. *Boundary Layer Meteorol.*, 17, 187–202.

Mahrt, L. and H.–L. Pan, 1984: A two–layer model of soil hydrology. *Bound. Layer Meteorol.*, 29, 1–20.

Mahrt, L., H.–L. Pan, P. Ruscher and C.–T. Chu, 1987: Boundary layer parameterization for a global spectral model. *AFGL–TR–87–0246. ADA199440.*

McFarlane, N. A., 1987: The effect of orographically excited gravity wave drag on the general circulation of the lower stratosphere and troposphere. *J. Atmos. Sci.*, 44, 1775–1800.

Mellor, G. L. and T. Yamada, 1982: Development of a turbulence closure model for geophysical fluid problems. *Rev. Geophys. Space Phys.*, 20, 851–875.

Miyakoda, K. and J. Sirutis, 1977: Comparative integrations of global models with various parameterization processes of subgrid scale vertical transport: Description of the parameterizations. *Beitr. Phys. Atmos.*, **50**, 445–487.

Miyakoda, K. J. Sirutis and J. Ploshay, 1986: One–month forecast experiments – without anomaly boundary forcings. *Mon. Wea. Rev.*, **114**, 2363–2401.

Palmer, T. N., G. J. Shutts and R. Swinbank, 1986: Alleviation of a systematic westerly bias in general circulation and numerical weather prediction models through an orographic gravity wave drag parameterization. *Q. J. R. Met. Soc.*, **112**, 1001–1039.

Palmer, T. N., C. Brankovic, F. Molteni, S. Tibaldi, L. Ferranti, A. Hollingsworth, V. Cubasch and E. Klinker, 1990: The European Centre for Medium–Range Weather Forecasts (ECMWF) program on extended–range prediction. *Bull. Amer. Meteor. Soc.*, **71**, 1317–1330.

Pan, H.-L. and L. Mahrt, 1987: Interaction between soil hydrology and boundary–layer development. *Boundary Layer Meteor.*, **38**, 185–202.

Pierrehumbert, R. T., 1987: An essay on the parameterization of orographic gravity wave drag. Geophysical Fluid Dynamics Laboratory/NOAA/Princeton University, Princeton, NJ 08542.

Schemm, J. K. E. and A. J. Faller, 1986: Statistical corrections to numerical prediction, Part IV. *Mon. Wea. Rev.*, **114**, 2402–2417.

Sela, J. G., 1980: Spectral modeling at NMC. *Mon. Wea. Rev.*, **108**, 1279–1292.

Sellers, P. J., Y. Mintz, Y. C. Sud and A. Dalcher, 1986: A simple biosphere model (SIB) for use within general circulation models. *J. Atmos. Sci.*, **43**, 505–531.

Shukla, J., 1981: 'Predictability of the tropical atmosphere' in report on Workshop on Tropical Meteorology and its Effects on Medium Range Medium–Range Weather Prediction at Middle Latitudes. ECMWF, 11–13 March 1981, pp. 21–51.

Slingo, J. M., 1980: A cloud parameterization scheme derived from GATE data for use with a numerical model. *Q. J. Roy. Meteor. Soc.*, **106**, 747–770.

Slingo, J. M., 1987: The development and verification of a cloud prediction scheme for the ECMWF model. *Q. J. Roy. Meteor. Soc.*, **113**, 899–927.

Tiedtke, M., 1983: The sensitivity of the time mean large scale flow to cumulus convection in the ECMWF model. Workshop on convection in large scale numerical models. ECMWF, 297–316.

Troen, I. and L. Mahrt, 1986: A simple model of the atmospheric boundary layer: Sensitivity to surface evaporation. *Boundary Layer Meteor.*, **37**, 129–148.

Wallace, J. M. and J. K. Woessner, 1981: An analysis of forecast error in the NMC hemispheric primitive equation model. *Mon. Wea. Rev.*, **109**, 2444–2449.

Wallace, J. M., S. Tibaldi and A. J. Simmons, 1983: Reduction of systematic forecast errors in the ECMWF model through the introduction of envelope orography. *Q. J. Roy. Meteor. Soc.*, **109**, 683–717.

Zhou, J., 1990: The impact of orographic representation effects and that of horizontal resolution in the AFGL–GSM on the short and medium range prediction. M. S. Thesis, Department of Meteorology, University of Maryland, College Park, MD.